Supplementary Materials for

Representation of Three-Dimensional Space in the Hippocampus of Flying Bats

Michael M. Yartsev and Nachum Ulanovsky*

*Corresponding author. E-mail: nachum.ulanovsky@weizmann.ac.il

This PDF file includes:

Materials and Methods
Figs. S1 to S22
References

Materials and Methods

Subjects and behavioral task

Five adult male Egyptian fruit bats, *Rousettus aegyptiacus* (weight 170–174 gr at implantation) were housed in a vivarium as described previously (*5*). Three bats were trained to fly in a large flight-room of a rectangular-cuboid shape (Experiment 1: Fig. 1A, room size 580 × 460 × 270 cm), searching for food (small pieces of banana) hidden in the eight arms of an artificial tree (Fig. 1A and fig. S1B). This design was inspired by our observations of the Egyptian fruit bats' natural behavior in the wild (ref. *29*), where bats feeding on fruit-trees performed complex flight maneuvers that resulted in dense three-dimensional (3D) coverage of the tree's surroundings (Fig. S1A, left; see also ref. *29*). Two additional bats, which received minimal (1-day) pre-training before surgery, were required to fly inside a cubic enclosure (Experiment 2: enclosure size 290 × 280 × 270 cm, Fig. S2A) and received food randomly inside the enclosure.

The entire flight-room was electromagnetically-shielded (enclosed in a large Faraday cage), and the room's walls and ceiling were covered with black acoustic foam, to minimize sonar reverberations; the floor was covered with black acoustically-absorbing felt. Experiments were done under relatively dim light conditions (illuminance 1–2 lux in cuboid-shaped setup; 0.5 lux in cubic enclosure; measured using ILT-1700 illuminance meter, International Light, MA). Egyptian fruit bats are a bat species which possesses good vision (*S1–S2*); this meant that our experimental bats likely performed the 3D foraging task using a combination of vision and echolocation.

Experiment 1 – Foraging in a rectangular cuboid flight-room: To measure 3D volumetric place-fields from hippocampal neurons, it is important to obtain good 3D flight coverage of the room's volume by the bat. We achieved this by encouraging the bats to search vigorously for the hidden food, as follows: (i) One piece of banana was placed inside one of the cups located at the ends of the tree's arms; these cups had high walls (~4 cm), which made it difficult for the bats to see the food inside the baited cup; (ii) Each of the eight cups, located at the ends of the eight arms of the tree, had an additional hidden compartment (below the main cup) which was baited with an additional piece of banana hidden under a mesh, such that in the eight arms of the tree there was only one accessible piece of banana and eight inaccessible pieces, which masked the odors of the accessible banana piece, and reduced the ability of the bats to localize the target food from a distance using olfaction; (iii) The 3D spatial positions of the eight arms of the tree were re-arranged each day to form a novel 3D configuration of the tree. Thus, bats had to physically search the individual arms of the tree, and fly around it vigorously, which resulted in complex flight trajectories (Fig. 1B and Fig. S3A). At the start and end of each recording day, the tree was thoroughly cleaned with water and with 70% ethanol, to remove odors. The arms of the feeding tree were re-baited during the session in case of food depletion, although on most recording days re-baiting of the feeders was rarely required. Bats were allowed to land only on the artificial tree or on curtains placed at two corners of the room. Despite the large size of the flight-room, bats were able to densely cover the room volume (Fig. S1C) by flying at high speeds (Fig. 1C and Fig. S4C, mean velocity: 106 ± 3 cm/s, peak velocity: 261 ± 15 cm/s, mean $\pm$ s.e.m.);

these high speeds allowed the bats to cover large distances during a single behavioral session (Fig. 1C, left; mean distance per session: 560 ± 40 m).

Experiment 2 – Foraging in a cubic flight enclosure: To corroborate our findings in another enclosure, single-unit neural activity was recorded in the hippocampus of two additional bats flying inside a nearly cubic flight enclosure ($290 \times 280 \times 270$ cm). This enclosure was constructed inside the original large flight-room, at one of the corners. Thus, two walls of the cubic enclosure were regular walls covered with black acoustic foam. The two additional walls of the cube were constructed of a frame of plastic rods and thick nylon wires which were densely packed (Fig. S2A; over 2-km of thick nylon wires were used to construct the enclosure; spacing between the vertical nylon wires varied between $0.25 – 4$ cm and was on average 1-cm) – but the inter-wire spacing allowed the 2 cameras to see through the walls and track the animal's position within this cubic enclosure. These 2 bats never explored outside of the cubic enclosure, and food rewards were available only inside the enclosure. Bats were rather unlikely to detect the far-away walls (beyond the wire-and-rod walls of the cubic enclosure) using echolocation, because: (i) The far-away walls were covered with acoustically absorbing foam, which attenuates sounds > 40 dB. (ii) Ultrasonic echolocation calls attenuate in air very rapidly with distance, within just a few meters, due to the very strong atmospheric attenuation at high frequencies (refs. *S1–S3*); the far away walls were 4–5 meters away, a total two-way acoustic travel distance of 8–10 meters, which meant atmospheric attenuation + spreading loss of 39–43 dB for 30-kHz sounds, the peak frequency of the echolocation clicks of these bats (*S4*) (attenuation compared to a distance of 10-cm from the bat's mouth). (iii) In contrast, the cubic arena was made of

highly-acoustically-reflecting materials: very thick nylon wires and large-diameter smooth plastic rods served as frame, all of which gave very strong echoes, which overshadowed any weak echoes from outside of the cubic enclosure. We conducted echo-return measurements (Fig. S2, D and E) to verify that indeed no detectable echoes return from the far-away walls. These measurements were done using a microphone and speaker positioned inside the cubic enclosure and facing outwards; microphone and speaker were positioned at a 1-meter distance from the nylon-and-rod enclosure wall, and 3.9-meters from the distal wall. Echo-return measurements were taken by playing wide-band sound pulses (5–100 kHz downward frequency-modulated sweeps) via an amplifier and an ultrasonic speaker; returning echoes were recorded using a wideband microphone positioned next to the speaker, and a wideband amplifier.

In the cubic-arena experiments, bats were also rather unlikely to perceive substantial light-reflection from the far-away walls using vision, because: (i) These cubic-arena experiments were conducted under dim light (0.5 lux). (ii) The acoustic foam on the far walls (which had black color) absorbed nearly all the incident light (97.6% light absorption for this black foam; Fig. S2B, right bar; light absorption was measured using a digital luminance meter and a calibration target with known light-reflectivity). Note that the amount of light reflected from this black-colored acoustic foam wall (100% – 97.6% = 2.4% light reflectance) was 34 times weaker than the amount of light reflected from a typical white-colored surface such as a laboratory wall (100% – 17.5% = 82.5% reflectance from a white surface; see Fig. S2B, left bar). (iii) In contrast, the thick wires and rods of the cubic-arena were densely packed (average 1-cm spacing), and these white nylon wires reflected strongly the light emitted by the bright light-emitting diodes on the

bat's head.   Thus, from the bat's perspective, the nylon-and-rods walls of the cubic

arena were seen as well-illuminated walls – in contrast to the black far-away walls which

reflected light very weakly, and were overshadowed by the nearby strong visual

reflectance of the cubic-enclosure walls (Fig. S2C).

During cubic-enclosure experiments, the bats were allowed to rest either on a

curtain hanging at the far corner of the enclosure (the corner farthest from the nylon-and-

rod walls) or on one of two polystyrene balls which were hanging from the ceiling and

served as resting platforms (no tree was used in the cubic enclosure). The location of the

curtain and hanging balls remained fixed across recording days. To encourage extensive

flight behavior, bats were subjected to a partial reinforcement strategy whereby they

received small amounts of banana pulp on the curtain or at the resting locations, after

randomly-selected flight epochs. Thus, the bats could not know a priori when and where

they would get the reward, which encouraged them to fly extensively and carry out

different flight maneuvers (Fig. S3B). Using this approach, the bats densely covered the

volume of the cubic enclosure (Fig. S6), by flying at high speeds (Fig. S4B, mean

velocity: 66 ± 0.6 cm/s, peak velocity: 146 ± 6 cm/s, mean $\pm$ s.e.m.; note they flew slower

than in the large rectangular-cuboid flight room, due to the smaller size of the cubic

enclosure). These high speeds allowed the bats to cover large distances during a single

behavioral session (mean distance per session in the cubic enclosure: 465 ± 41 m).

In both experimental setups, two sleep sessions flanked the behavioral session:

sleep $\rightarrow$ behavior $\rightarrow$ sleep. The behavioral session consisted of one uninterrupted period

of time, during which the bat was required to fly within the rectangular flight-room (in

experiment 1) or the cubic enclosure (in experiment 2). The duration of the behavioral

session was variable and often continued until proper coverage of the flight-room was obtained: this depended on the bat's flight speed and active behavior. Typically, the duration of behavioral sessions was ~30 min (average: 31.8 ± 6.9 min in the cuboid flight room; 26.2 ± 7.4 min in the cubic flight enclosure; mean $\pm$ s.t.d. over all the recording days in each enclosure, respectively). The durations of the sleep sessions were more constant and typically lasted 10 minutes. During the sleep sessions, the bat was comfortably placed inside a holding bag, with its head and neck outside of the bag, and rested on a pedestal inside the flight room. Throughout the duration of the recording (2 sleep sessions + behavioral session), the bats were not taken outside of the recording room, and the recording was run continuously (see below more information on recording methods).

Experimental procedures were approved by the Institutional Animal Care and Use Committee of the Weizmann Institute of Science.

Video and audio recordings

The bat's position was recorded using two video trackers, connected to two cameras placed at two of the upper corners of the flight-room (Fig. 1A), which tracked the position of two light-emitting diodes connected to the head-stage on the bat's head (Fig. S10). Positional data were collected and stored with a 25-Hz sampling rate. The bat's 3D position in the flight room was reconstructed using the direct linear transform algorithm, applied to the data from the two cameras, similar to the method described previously (*S3 –S5*). We included in the analysis only valid video frames for which video data were available from both cameras (i.e., the bat was within the field of view of both cameras,

with no occlusions from either camera). If segments of video data were missing, we interpolated the video data using cubic spline; if the missing segment was longer than 280 ms, we extrapolated only up to 280 ms from the last valid video frame (i.e., extrapolation over 7 video frames; we verified that cubic-spline extrapolation follows faithfully the bat's trajectory over such short time periods of 280 ms). 3D locations within the flight-room were calibrated using 246 calibration points which spanned the volume of the room, and whose positions were measured with a precision of 0.5 mm using a laser-ranging theodolite; this large number of calibration points allowed achieving a median positional reconstruction accuracy of 12-mm across the room. Reconstruction accuracy was estimated using a leave-one-out algorithm, in which every point was reconstructed based on the remaining 245 calibration points. Additional calibrations were conducted at least once a week to validate the stability of the cameras and ensure that the reconstruction accuracy of 3D positions was maintained throughout the recordings.

The timing of the bat's echolocation calls was recorded by filtering a 31–39 kHz frequency slab, and heterodyning it down in frequency to 0–8 kHz using two bat-detectors placed on the floor of the flight-room and facing the room center (Fig. 1A), and then sampling the signal continuously at 16 kHz. The heterodyning distorted the detailed structure of the echolocation calls, but permitted an accurate measurement of call timing (*3-5*). Echolocation calls in this bat species occur in characteristic double-clicks with 20-ms intervals (*5, 27, S1–S7*); these clicks were detected offline via a threshold-crossing algorithm (*3-5*). Clicks with intervals under 30-ms were merged, to avoid contamination by returning echoes that may cross the detection threshold. This resulted in each double-click being counted as one call; hence, the autocorrelograms and cross-correlograms of

the bat sonar calls shown in Fig. S20 refer to the merged double-clicks.   On a small portion of the recording days in the rectangular cuboid flight-room, the sensitivity of the bat detector was set too high, which did not allow accurate detection of the echolocation clicks; these days (n = 3 days) were discarded from the analyses related to the echolocation signal.   Audio recordings from the cubic enclosure were not considered here because the microphones in this small enclosure were positioned rather close to the bat and hence the audio signal may have been contaminated by mechanical noises resulting from the bat's wings hitting on the plastic protector of the recording device.

Surgery

All anesthesia and surgical procedures followed those described previously in detail for hippocampal CA1 implants in Egyptian fruit bats (*5*). Briefly, upon completion of the behavioral training, the bats underwent surgery to implant a 4-tetrode microdrive. Following induction of anesthesia using an injectible anesthesia cocktail of ketamine 15 mg/kgBW and medetomidine 0.06 mg/kgBW, the bat was placed in a stereotaxic apparatus and anesthesia was maintained throughout surgery by isoflurane (0.25 – 3%, as needed) in 98% oxygen.

Bats were implanted with a four-tetrode lightweight microdrive (4-drive; weight 2.1 gr). Tetrodes (~45 μm diameter) were constructed from four strands of platinum-iridium wire (17.8 μm diameter, HML-insulated), bound together by twisting and then melting their insulations; tetrode wires were gold-plated on the day before surgery to reduce their impedance to 300–700 kΩ. While the bat was under isoflurane anesthesia, a circular opening (craniotomy of 1.8-mm diameter) was made in the skull over the right

hemisphere. Center of craniotomy was positioned 3.5– 3.75 mm lateral to the midline and 5.5 mm anterior to the transverse sinus that runs between the posterior part of the cortex and the cerebellum. The microdrive was placed vertically to allow the tetrodes to move perpendicular to the CA1 pyramidal layer. A bone screw with a soldered stainless-steel wire was fixed to the skull in the frontal plate, and served as a ground screw, after its electrical connection to the dura was verified.

Electrophysiological recordings

During a period of ~1 week after surgery, the tetrodes were slowly lowered towards the CA1 pyramidal layer. In all cases, one of the tetrodes served as a reference electrode and was left in an electrically-quite zone in the white matter above the CA1 pyramidal cell layer; we periodically verified the reference tetrode was still electrically-quiet, by examining its activity against the ground screw.

The position of tetrodes in the CA1 pyramidal cell layer was provisionally determined by the presence of high-frequency oscillations (ripples) in the local field potential via daily connecting of the bat to the tethered (wired) recording system, while the bat was sleeping (or during quite wakefulness); tetrode positioning was subsequently verified histologically. Recording tetrodes were never kept in the same position, and were moved at the end of each recording session (40–160 μm daily), in order to obtain recordings from new ensembles of neurons.

During flight, neural activity from a single tetrode (4 channels) was recorded using a custom, lightweight 4-channel neural telemetry system (Fig. 1, D to G). This system was designed specifically for recording in fast-flying animals, and has several

10

requisite characteristics: It has long transmission range (50 meters); signal quality is not hampered by rapid motion or accelerations; and it is lightweight (see below). Jumper-wires on the telemetry headstage allowed choosing which tetrode to transmit, and thus every day we connected the bat to a regular wired recording system and chose the tetrode with best-quality spikes to be transmitted on that day. The neural signals on the 4 channels of that tetrode were amplified and filtered at 300–6,000 Hz, and then transmitted wirelessly. We implemented the 300-Hz high-pass filter before transmission because of the properties of the telemetry receivers, that could not track modulated signals below 70 Hz – which meant that, with this system, we could not record local-field potentials; therefore, we further high-passed the signal in hardware with a corner frequency of 300-Hz, before transmission, to improve the dynamic range of the spike recordings. The telemetry transmission was based on an analog wideband frequency modulation (W-FM), with each of the 4 channels of the tetrode being transmitted at a different carrier frequency (highly stable carrier frequencies, in the range of 912 – 925 MHz). The signal was picked up by two antennas, equipped with low-noise radio amplifiers, which were located at two corners of the flight-room (Fig. 1A). The two antennas allowed redundancy in choosing which of the radio signals had higher quality; for every recording day, we analyzed data from only one of the antennas, the one that had the best signal-to-noise ratio and the least artifacts. The radio signal was demodulated by eight FM receivers (8 receivers for the 4 neural channels × 2 antennas), and was then sampled continuously at 30.3 kHz and stored to disk for offline processing. Because of the 300-Hz high-pass filtering of the telemetry transmitter and the 70-Hz high-pass

filtering of the telemetry receivers, it was not possible to record local field potentials; rather, only spikes were recorded.

The telemetry system weighted ~12 gr (including headstage, amplifier, transmitter, battery, and plastic casing) and was attached to a connector on top of the 4-tetrode microdrive (Fig. 1F and Fig. S10). The Egyptian fruit bats, which weighed 170–174 gr, carried this weight with ease, as expected from our previous experiments in the wild (*29*), whereby: (i) Males of the same bat species carried a GPS device of similar weight (up to 13 gr) while flying up to ~100 km over a single night (*29*); and (ii) Females of this species, which have a smaller weight than males, can fly while carrying on them pups weighing up to ~50 gr (N.U., personal observations) – 4 times heavier than our telemetry system.

The telemetry system had a broad-band frequency range, appropriate for recording spikes (< 6 dB attenuation for spike frequencies, Fig. S9, A to C); it had a very linear amplitude response for input signals from 0 to ±300 μV, covering the range of typical spike amplitudes (Fig. S9, D and E); and it exhibited very low system noise (4–7 μV internal system noise after transmission, Fig. S9F). To test the system, we conducted simultaneous tethered and wireless recordings, using both synthetic signals (Fig. S8) and neural signals (Fig. 1, D and E; and Fig. S7), which verified the quality of the wireless signal throughout all the locations in the flight-room. During daily recordings, the wireless data were collected continuously throughout all the behavioral and sleep sessions of each recording day (sleep → behavior → sleep; ~1 hour daily; the battery of the telemetry transmitter could last ~2 hours or more without re-charging).

Artifacts in the neural signal, resulting from the bat's wings hitting on the transmitter (Fig. S11), were detected using a threshold-crossing algorithm, with threshold set slightly higher than the maximal amplitude of spikes recorded during the flanking sleep sessions. Artifacts were easily distinguishable from spikes, based on the large amplitudes of the artifacts and their characteristic shape (Fig. S11A). The occurrence and amplitude of artifacts were experimentally minimized using mechanical dampers, which included light-weight plastic protectors that prevented direct contact between the bat's wings and the electronics, and silicon rubber that cushioned the bottom part of the light-emitting diodes. Artifacts comprised, on average, $3.6 \pm 0.91\%$ of the total flight time; importantly, the fraction of the time taken by artifacts decayed drastically over recording days, as the bats gradually learned to adjust their wing-stroke to prevent hitting the transmitter with their wings (Fig. S11D).

Spike sorting

The recorded continuous neural signals were filtered digitally offline between 600–6,000 Hz, and spike waveforms were extracted by threshold-crossing. Spike sorting was conducted as described previously (*3-5*). Waveforms were spike-sorted on the basis of their relative energies and amplitudes on different channels of the tetrode. A clustering software was used to isolate clusters of single units. Each spike was graphically positioned in a two- or three-dimensional graph representing the energy or amplitude of the spike on two or three of the tetrode's four channels. Convex hull boundaries and template-matching of waveforms were used to identify well-separated clusters of spikes, which were individually color-coded. Data from all three sessions (behavioral + two

sleep sessions) were spike-sorted together. Finally, the quality of cluster separation was verified by computing the 'isolation distance' index (*5, S8–S10*), a standard index commonly used in rats, which calculates the distances between spike clusters of different cells in Mahalanobis space using principal components and spike-energy features (*S8*). The median isolation distance for CA1 neurons in flying bats was 30.1 (18.4 – 47.3 interquartile range). These values are similar to those reported previously for recordings from the hippocampus of rats (*23, S9*) and bats (*5*).

Overall, we recorded a total of 139 well-separated neurons from the dorsal hippocampal CA1 region of five bats (94 neurons from 3 bats foraging in the rectangular cuboid flight-room, and 45 neurons from 2 bats foraging in the cubic enclosure). Well-isolated hippocampal neurons recorded during flight were identified as complex-spike cells (putative pyramidal neurons) as follows: First, the waveform of each neuron had a characteristic shape with a narrow peak followed by a long after-hyperpolarization trough (Figs. 1D and 2A). Second, the mean firing rate over all three sessions was < 5 Hz. Third, analysis of the neuron's inter-spike interval histogram for the entire recording session, as well as during epochs of flights only, revealed a tendency to fire in complex-spike bursts, as evidenced by the bimodal shape of the interval histogram, with a clear peak at short inter-spike intervals of 5–10 ms (Fig. S22). The tendency of bat CA1 neurons to emit complex spikes in flight (Fig. S22A) was similar to the complex-spiking of CA1 neurons during crawling (Fig. S22B; see also refs *3-5*). Interneurons were typically not recorded during flight.

For all subsequent analyses we only used well isolated (single-unit) pyramidal neurons which were behaviorally active, i.e. (i) fired more than 40 spikes during flight,

and (ii) had a mean firing rate > 0.15 Hz during flight. A substantial fraction of the CA1 neurons were 'behaviorally silent' cells, i.e. were active during the rest periods but not active during flight behavior (66/139 neurons were 'behaviorally silent cells'; 47.5% of total cells). A total of 73 well-isolated neurons from hippocampal area CA1 were defined as 'behaviorally active during flight', and were included in the analyses below (44 neurons from 3 bats foraging in the rectangular cuboid flight-room, and 29 neurons from 2 bats foraging in the cubic enclosure).

Data analysis

Firing-rate maps and definition of place cells

All data analysis was conducted in Matlab. The same analysis procedures were applied to all cells, from both the rectangular cuboid flight-room and the cubic enclosure. Firing-rate maps were constructed for flight periods only. Individual flights were identified as time-epochs during which the bat's 3D velocity was higher than 25 cm/s for a duration of at least 1-s (see example in Fig. S11C; dashed horizontal gray line shows the 25 cm/s threshold). To improve the accuracy in estimating flight velocity, the bat's position was smoothed using a smoothing spline (*csaps.m* in Matlab), based on which the instantaneous velocity was extracted. Further, the first and last 1-s segments of each flight epoch were removed to ensure that the take-off and landing data did not contaminate the pure-flight epochs, due to the smoothing of the bat's velocity.

To compute 3D place fields, the 3D volume of the flight room was partitioned into $10 \times 10 \times 10$ cm^3 voxels, and the rate-maps were computed using an adaptive

15

smoothing algorithm. This adaptive smoothing (adaptive binning) approach was similar to the adaptive smoothing procedure used previously to compute place fields in rats running in two-dimensional (2D) environments (*12*, *S11*), and it was used here (similarly to the rat studies [*12*, *S11*]) in order to optimize the trade-off between blurring error and sampling error, and thus to compensate for the non-uniform behavioral coverage of the flight room. Specifically, the volume of each voxel was gradually increased until the amount of time-spent within that voxel exceeded 1 second. The number of spikes within the extended voxel was then divided by that time-spent (~1-s for all voxels) to derive the firing-rate. We excluded all the $10\times10\times10$ cm^3 voxels whose center was located more than 30 cm from the actual flight trajectory of the bat, in order to avoid the admission of un-visited voxels into the analysis due to the adaptive smoothing procedure. The resulting 3D rate map was further smoothed using a $30\times30\times30$ cm^3 filter; this corresponds to a very minimal smoothing with a $3\times3\times3$-voxels filter, i.e., only one bin on each side. (Similar results were obtained using fixed voxel size, but this approach yields much noisier place-fields, that were also oftentimes split; hence we used in this study the adaptive-smoothing procedure, similar to that used previously in rats [*12*, *S11*]).

The spatial information, in bits per spike (*3-5*, *12*, *S11–S12*), was calculated for each neuron as:

spatial information (bits/spike) $= \sum p_i \, (r_i \, / \, r) \, \log_2(r_i \, / \, r)$

where r_i is the firing rate of the neuron in the *i*-th voxel of the place-field, p_i is the probability of the animal being in the *i*-th voxel (time spent in *i*-th voxel / total flight time in the session), $r = \sum p_i \, r_i$ is the overall mean firing rate during flight, and *i* is running

over all the voxels.   We also computed the 'sparsity' index for individual neurons, as described previously (*3-4*, *S11*), using the following formula:

$$Sparsity = \frac{\langle r_i \rangle^2}{\langle r_i^2 \rangle} = \left(\sum p_i r_i \right)^2 / \sum p_i r_i^2$$

where p_i and r_i are as defined above.   Distributions of spatial information and sparsity are shown in Fig. S12.   The spatial information per spike was used as our primary measure to determine whether a neuron was a place-cell or not. To assess the significance of the spatial information value obtained for each neuron, we compared the actual spatial information value to the spatial information values computed for a set of shuffled spike trains, as follows: The shuffled distribution was generated by randomly distributing the timestamps of the spikes (same amount of spikes as in the original spike-train) between all the flight epochs of the behavioral session, while making sure that shuffled spikes would occur only during valid periods of data (i.e., making sure that the true number of spikes would occur only during valid video frames and artifact-free periods of time). This shuffling procedure was repeated 1,000 times for each neuron. For each repetition, the firing-rate maps were computed in the same manner as described above, and the spatial information index was then computed. Neurons whose spatial information index exceeded the upper boundary of their shuffled-distribution 95% confidence interval, i.e. which showed a spatial information index higher than would be expected by chance, were defined as place-cells (Fig. S12A, white bars). Of the behaviorally-active cells, 75% (55/73 cells) were classified as place cells (35 place-cells from 3 bats foraging in the rectangular cuboid flight-room and 20 place-cells from 2 bats foraging in the cubic enclosure).

We also analyzed for Fig. 4 (D and E) and for Figs S18 and S19 the dataset of hippocampal CA1 place-cells that we previously recorded from 2 Egyptian fruit bats crawling in 2D (n = 23 cells recorded in crawling bats, which were reported in our previous study (*5*); for the crawling data, place cells were classified as neurons with spatial information > 0.5 bits/spike).

3D place-field analysis

A 3D place field was defined as a contiguous region of $\geq$ 64,000 cm^3 (equivalent to $\geq$ 40×40×40 cm^3) where the firing rate was above 50% of the peak firing-rate of the neuron. The number of non-overlapping place fields was assessed for each cell (Figs. 2K and 3, A to F). A place-field was considered valid if the neuron emitted spikes within the field during at least two different flight passes. In the rectangular cuboid flight-room, a total of 55 place fields were found for the 35 recorded place-cells (Fig. 3E), with each place-cell exhibiting typically 1 or 2 place fields, and more rarely 3 or 4 fields (Fig. 3E). In the cubic enclosure, a total of 27 place fields were found for the 20 recorded place-cells (Fig. 3F), with each place-cell exhibiting typically 1 or 2 place fields, and only one neuron had 3 firing fields (Fig. 3F). Place cells in the rectangular-cuboid flight room had a larger number of multiple fields (more than one place-field) than in the cubic enclosure (compare Figs. 3E versus 3F). To test whether the fraction of place-cells with multiple fields was indeed significantly larger in the rectangular-cuboid flight room, we employed a bootstrap procedure where we randomly pulled the same number of place-cells (35 for the cuboid flight-room and 20 for the cubic enclosure) with repetitions from the original data set, and computed the fraction of cells with more than a single field in each setup.

This procedure was repeated 1,000 times for each setup and resulted in two distributions, which were then compared using a standard *t-test* – which indeed confirmed that the fraction of place-cells with multiple fields was significantly larger in the rectangular-cuboid flight room then in the cubic enclosure ($P < 0.001$).   The size of each individual place-field was computed in each dimension by taking the extent of the central 95th percentile of that place-field's voxels along that dimension. We also computed the overall average size for each place-field, by taking the mean of the three *x,y,z* sizes (average across the three individual *x,y,z* dimensions); these are the values that were plotted in Fig. 3J.

We tested whether the firing-fields of hippocampal place cells had an isotropic shape, by fitting each place-field with an ellipsoid and extracting the diameter of the ellipsoid's three axes. An 'elongation index' (Fig. S16) was defined as the ratio between the diameter of the longest axis (*c*) and that of the shortest axis (*a*):

$$elongation\_index = \frac{c}{a}$$

We then tested whether the elongation index computed for each place-field was statistically different from that expected from a spherical shape, by applying a shuffling procedure, as follows: First, for each field, we defined a perfect sphere whose center matched the center of the fitted ellipsoid and whose diameter equaled the geometric mean of the ellipsoid's three full-axes ($d = \sqrt[3]{abc}$) – so that the volume of the sphere was identical to the volume of the original ellipsoid. Second, the spikes within each field were randomly distributed over the flight-trajectories that passed inside the sphere, and then the shuffled place-field was calculated, and its elongation index was computed in the same way as described above. This shuffling procedure was repeated 100 times for each

place-field. Place fields whose elongation-index exceeded the upper boundary of their shuffled-distribution 95% confidence interval, i.e. which had an elongation-index higher than that expected by chance from an underlying spherical field, were defined as non-spherical, or non-isotropic place-fields (these fields are marked by red dots in Fig. 3I and Fig. S17C). We examined also an alternative definition for the 'elongation index', whereby we defined it as the ratio between the diameters of the longest axis (*c*) and the mean of the two remaining axes (*a* and *b*); this yielded similar results. Furthermore, we tested also the effect of using a lower firing-rate threshold for extracting the place-fields, which yielded similar results: Specifically, for our standard firing-rate threshold (50% of the peak firing-rate), 91% of the 3D place-fields were not significantly different from a sphere – while for the alternative firing-rate threshold (25% of the peak firing-rate), 87% of the 3D place-fields were not significantly different from a sphere.

Place field stability

Firing-rate maps show the mean firing-rate value for each voxel in the room, but do not provide information on the temporal dynamics, such as whether the firing pattern is stable across the entire session. We assessed the stability of the 3D place-fields of hippocampal place cells in two ways. First, we calculated a voxel-wise correlation coefficient between the two firing-rate maps computed for the odd minutes versus the even minutes of the recording session (Fig. S14). Second, we calculated a similar voxel-wise correlation coefficient between the two firing-rate maps computed for the first versus second halves of the recording session, as was done previously in rats (*22*) (Fig. S14). For each of these partitions of the full data, we analyzed two populations of place-cells: (i) All place-cells (which, as part of their definition, emitted ≥ 40 spikes during the entire session), and (ii)

20

place cells that fired ≥ 40 spikes for each of the two partitions of the session (i.e., cells with at least 80 spikes in the entire flight session, and usually more) (Fig. 2, C and D; and Fig. S14). We assessed the stability (correlation coefficient) of the place-fields using the 3D rate-maps as well as using all the 2D projections of the rate maps on pairs of major axes (Fig. 2, C and D; and Fig. S14).

Analysis of spike-train theta modulation

To assess the degree of theta modulation in the spiking patterns of place-cells recorded in bat CA1 (Fig. 4 and Figs. S18 and S21), we analyzed the spike-train temporal autocorrelograms, as described previously (*5*). Bin size of all the temporal autocorrelograms was 10 ms (other bin sizes were tested, and yielded similar results). The autocorrelogram was computed for $\pm$ 500-ms lags, and the peak of the autocorrelogram at zero lag was equalized to the maximal value not including the zero-lag peak (*23*, *24*, *S10*). The power spectrum of the temporal autocorrelograms was assessed by removing the mean of the autocorrelogram and computing the fast Fourier transform (FFT) of this mean-normalized (mean removed) autocorrelogram, and then calculating the square of the FFT magnitude; the length of the FFT was zero padded to 2^{16}. The power spectrum was smoothed with a 2-Hz rectangular window, and the peak value within the 5–11 Hz band was identified. A 'theta-index' was defined for each neuron as the ratio between the mean power within 1-Hz of each side of the peak in the 5–11 Hz frequency range, and the mean spectral power between 0 Hz and 50 Hz. This definition is similar to the 'theta index' used previously in rodents and bats to identify theta modulation of grid-cells (*5*, *23*, *24*, *S10*, *S13*) and place cells (*23*, *24*). To assess the significance of the theta-index, we compared the actual theta-index value to a set of

shuffled spike-trains, as follows: The shuffled distribution was generated by randomly distributing the timestamps of the spikes (same amount of spikes as in the original spike-train) between the different flight-epochs, while making sure that the spikes would occur only during valid periods of data (i.e., that the true number of spikes would occur only during valid video frames and artifact-free periods of time). We then re-computed the theta index for each realization; this shuffling process was repeated 1,000 times per neuron. Neurons whose theta-index exceeded the upper boundary of their shuffled-distribution 95% confidence interval, i.e. which showed a theta-index higher than would be expected by chance, were defined as 'theta-modulated' (these neurons are marked by red dots in Fig. 4C and Figs. S18 and S21). Following this procedure we found that of the 55 place-cells recorded in both experimental flight setups, only 2 place cells were significantly theta-modulated (2/35 place cells in the cuboid flight room and 0/20 cells in the cubic flight enclosure; Fig. 4C).

We further tested whether this number of cells that passed the significance threshold was greater that would be expected by chance. We tested the hypothesis at the population level and asked what is the probability to get m or more cells, out of N place cells, with a significant ($p < 0.05$) theta index, assuming independence. We employed the binomial test using the following formula:

$$p_{\text{value\_population}} = \sum_{i=m}^{N} p^i (1-p)^{N-i} \frac{N!}{i!\,(N-i)!}$$

where N is the total number of cells (in our data: $N = 55$ place-cells), p is our per-neuron significance threshold for defining a cell as being 'theta modulated' (in our data: $p = 0.05$, see above), and m is the number of significantly theta-modulated cells (in our data: $m = 2$ significant cells, see Fig. 4C, red dots). Thus, we asked whether getting $m = 2$ cells that

22

are each theta-modulated at the $p < 0.05$ significance level, out of a total of $N = 55$ place cells, is greater than would be expected by chance. The population-wise p value ($p_{value\_population}$) obtained by this procedure was: $p = 0.77$, which is not significant; that is, the number of 'theta-modulated' place cells that we found (2/55 cells) was not greater than would be expected by chance.

Histology

Histology was done as described previously (*5*). In brief, tetrodes were not moved after the final recording session. The bats were anesthetized, and electrolytic lesions (DC positive current of 30 µA, 15-s duration) were done to assist in the precise reconstruction of tetrode positions. Immediately after doing the lesions, the bat was given an overdose of sodium pentobarbital and, with tetrodes left *in situ*, was perfused transcardially using a flush of 50 ml phosphate buffer saline followed by 200 ml of fixative (4% paraformaldehyde + 0.1 M phosphate buffer saline). The brains were removed and stored in fixative. Subsequently, a coronal block was embedded in paraffin, and then 10 µM coronal sections were cut; every 3rd section was mounted on glass slides, resulting in 30 µM intervals between adjacent mounted slides. The sections were then Nissl-stained with Cresyl violet, and coverslipped. A light microscope fitted with a digital camera was used to determine tetrode placement in the CA1 pyramidal layer of dorsal hippocampus.

A

Zoom-in: Dense 3D foraging of the bat around the fruit tree (side view)
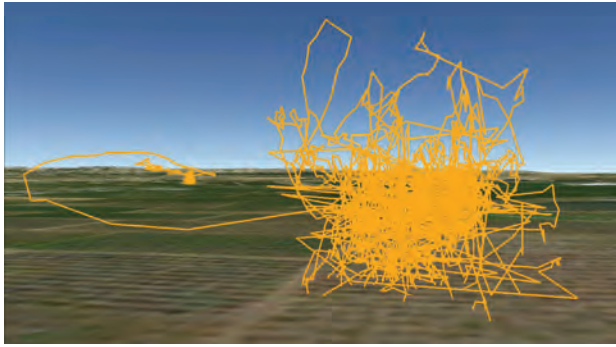
Zoom-out: Flight from cave to fruit tree (top view)

5 km

B   Laboratory flight room
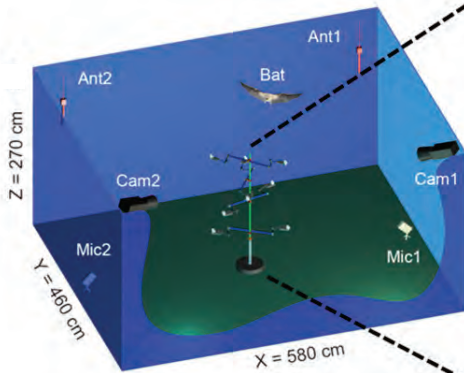
Laboratory feeding tree

Ant1

Ant2

Bat

Z = 270 cm

Cam2

Cam1

Mic2

Mic1

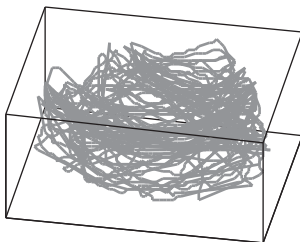Y = 460 cm

X = 580 cm

C

3D view

XY

YZ

XZ
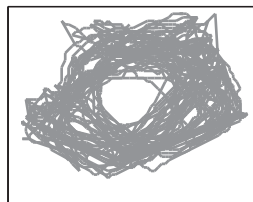
Fig. S1. Experimental setup #1: Rectangular cuboid flight room.

The design of the 3D naturalistic foraging task used in this study (in the rectangular-cuboid flight room) was inspired by the bat's natural behavior in the wild, as reported in our previous work (ref. *29*), where we observed that Egyptian fruit bats densely cover the 3D surroundings of the feeding-tree during a single feeding session (ref. *29* and panel **A**, left). Therefore, for the current study we designed and constructed an artificial feeding-tree (panel **B**), in order to encourage a 3D tree-foraging behavior similar to that observed in the wild. This tree had 8 maneuverable arms and it was placed in the center of the flight-room, with food placed randomly in one of the tree's arms, to motivate the bats to densely cover the 3D volume of the room (ref. *19*; see also Fig. 1B).

Continued on next page

Continued from previous page

(**A**) Bat foraging flights to and around a real fruit-tree in the wild. Right: Example of a single nightly flight trajectory of one bat that was tracked with a miniaturized GPS datalogger (ref. *29*). This bat flew from its cave (green triangle) via a straight flight-trajectory (orange line) to a feeding tree (red circle), where it foraged on fruits for several hours, and then flew back to its cave. Data are from Tsoar, Nathan, Bartan, Vyssotski, Dell'Omo and Ulanovsky (ref. *29*). Flight data are superimposed on an aerial photo of the tree's surroundings, taken from Google Earth (the Google Earth images depict daylight, although in reality the bat flew during the night). Left: Zoom-in on the feeding site, showing the bat's flight trajectory while foraging on the fruit-tree. Note the dense 3D coverage around the tree, and the complex 3D flight maneuvers.   (**B**) Bat foraging around an artificial "fruit-tree" in the laboratory. Left: Egyptian fruit bats were trained to fly freely in a large flight-room (580 x 460 x 270 cm), searching for food hidden in the arms of an artificial tree placed in the center of the room. cam1,2: cameras; mic1,2: ultrasonic microphones (bat detectors); ant1,2: receiving antennas for neural-telemetry signal. The room, tree and bat are drawn to scale; cameras, antennas and microphones were enlarged here for display purposes. Right: Zoom-in on the artificial tree placed in the center of the flight-room.   (**C**) Example of flight-room coverage during a single recording session; shown are a 3D display and 2D projections. Hole in middle of XY projection corresponds to the location of the tree. This is a representative example in terms of total distance flown in the cuboid setup (was 607-m here compared to 560-m population average).
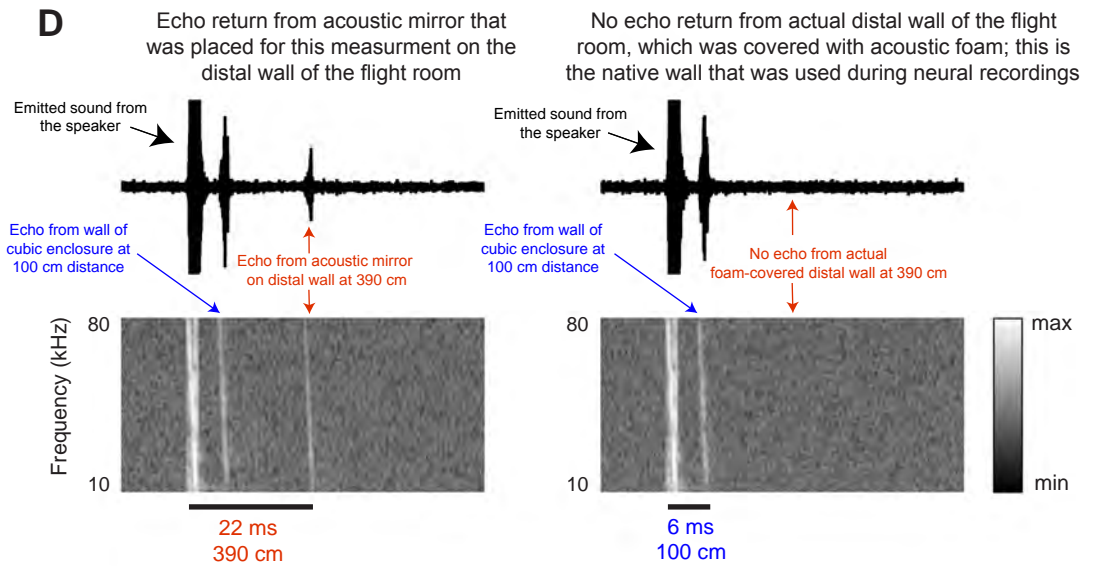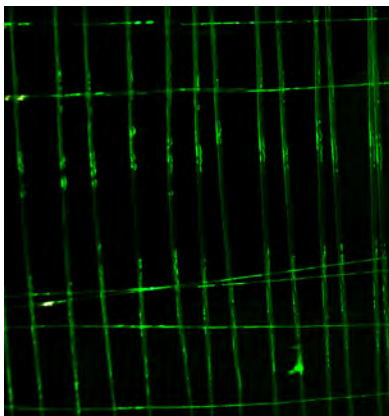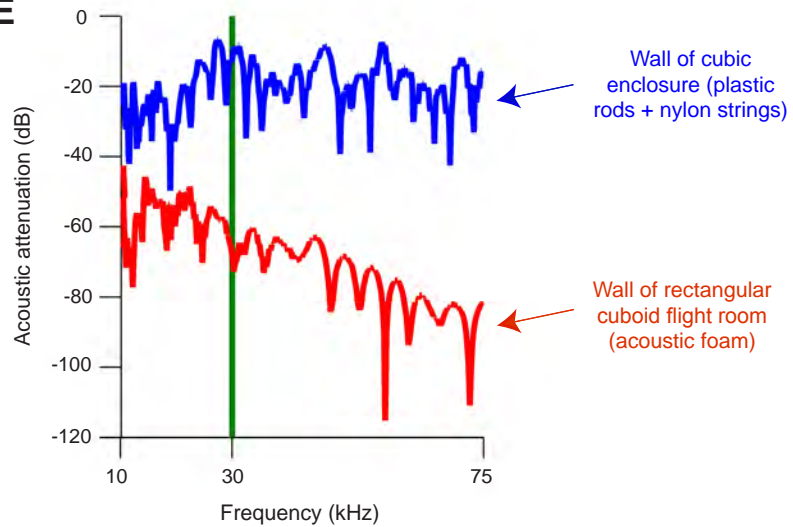
A

B

C

D

Echo return from acoustic mirror that was placed for this measurment on the distal wall of the flight room

No echo return from actual distal wall of the flight room, which was covered with acoustic foam; this is the native wall that was used during neural recordings

Emitted sound from the speaker

Echo from wall of cubic enclosure at 100 cm distance

Echo from acoustic mirror on distal wall at 390 cm

22 ms
390 cm

Emitted sound from the speaker

Echo from wall of cubic enclosure at 100 cm distance

No echo from actual foam-covered distal wall at 390 cm

6 ms
100 cm

E

Wall of cubic enclosure (plastic rods + nylon strings)

Wall of rectangular cuboid flight room (acoustic foam)

Fig. S2. Experimental setup #2: Cubic enclosure.
(A) Bats (n = 2) were flying inside a cubic flight enclosure of nearly identical dimensions (290 x 280 x 270 cm), which was constructed at one of the corners of the original large cuboid flight-room. Thus, two walls of the cubic enclosure were regular walls covered with black acoustic foam. The two additional walls of the cube were made of densely packed thick nylon wires and plastic rods (spacing between the vertical nylon wires varied between 0.25 – 4 cm and was on average 1 cm; horizontal nylon wires were added, too). Experiments in this enclosure were conducted under dim light conditions (0.5 lux). **(B to E)** Bats were unlikely to detect substantial reflections from the distal walls of the room, using either vision or echolocation. **(B)** The ceiling and distal walls of the large room were covered entirely with black-colored acoustic foam, and the floor was covered with acoustically-absorbing black felt, and hence were difficult to detect using vision, compared to the visually highly reflective walls of the cubic enclosure (see below). The black opaque color of the acoustic foam on the far walls absorbed nearly all the incident light: 97.6% light absorption for this black foam (panel B, right bar; see (*19*)). **(C)** Photograph illustrating that the green light-emitting diode (the same type that was connected to the bat's head during neural recordings) created strong light reflections from the dense nylon-wires of the cubic-enclosure walls – but there was essentially no light reflection from the distal walls of the room covered with black acoustic foam (i.e., the distal wall was nearly invisible compared to the cubic-arena walls). **(D and E)** Echo-return measurements.
(D) Figure D-left shows an example of returning echoes (top, waveform; bottom, spectrogram [frequency x time] of the sound), taken under a condition where we added an acoustic mirror (large Perspex plate) on the distal room wall, to counter the > 40 dB attenuation of the acoustic foam (*19*). As expected, two strong returning echoes were then detected (following the emitted sound from the speaker), one echo from the nylon-and-rod wall of the cubic enclosure, arriving after 6 ms from sound emission (blue arrow, corresponding to an object at 100-cm = distance to the cubic-arena wall); and another echo from the acoustic mirror positioned on the distal wall, arriving after 22 ms from sound emission (red arrows, corresponding to an object at 390 cm = distance of the Perspex plate; see (*19*)). When the same experiment was conducted under the native condition, i.e. without the acoustic mirror (D-right) – that is, under the actual conditions of the neural recordings, when the far wall was fully covered with acoustic foam – the returning echo from the far wall (at 390 cm distance) was totally absent, due to the > 40 dB attenuation of the sound by the acoustic foam. Thus, the echoes from the distal wall in the actual experiment were practically non-existent compared to the strong echoes from the nylon-and-rod walls of the cubic arena. Note that in these plots, the left-most signal (strongest signal) corresponds to the emitted sound pulse from the speaker; it has been clipped for display purposes only. **(E)** Acoustic target-strength measurements: Quantification of the attenuation of sound echoes from the distal wall – a wall that was covered with acoustically-absorbing foam – compared to the echoes from the nylon-and-rod wall of the cubic arena. Data are plotted for the frequency range of Egyptian fruit bat's natural echolocation calls (10–75 kHz). We measured the acoustic target-strength by performing echo-return measurements of the acoustic foam at 100-cm distance, compared to the nylon-and-rod walls of the cubic arena at 100 cm, and then correcting for the atmospheric attenuation and spreading loss at a 390-cm distance, as done previously (*S3-S5*). Note the dramatic difference in target strength between the highly-reflective walls of the cubic enclosure (blue line) compared to the distal strongly-absorbing walls of the cuboid flight room (red line): For example, at the frequency of main energy of the echolocation calls of Egyptian fruit bats, 30 kHz (green vertical line) – the target strength (echo power) from the highly-reflective walls of the cubic enclosure was > 55 dB stronger than the echoes from the distal room walls covered with acoustic foam. Thus, any echoes from the walls outside of the cubic enclosure were over-shadowed by the highly reflective walls of the cubic enclosure.

Supplementary Figure 3

A   Rectangular cuboid flight room (580 x 460 x 270 cm)

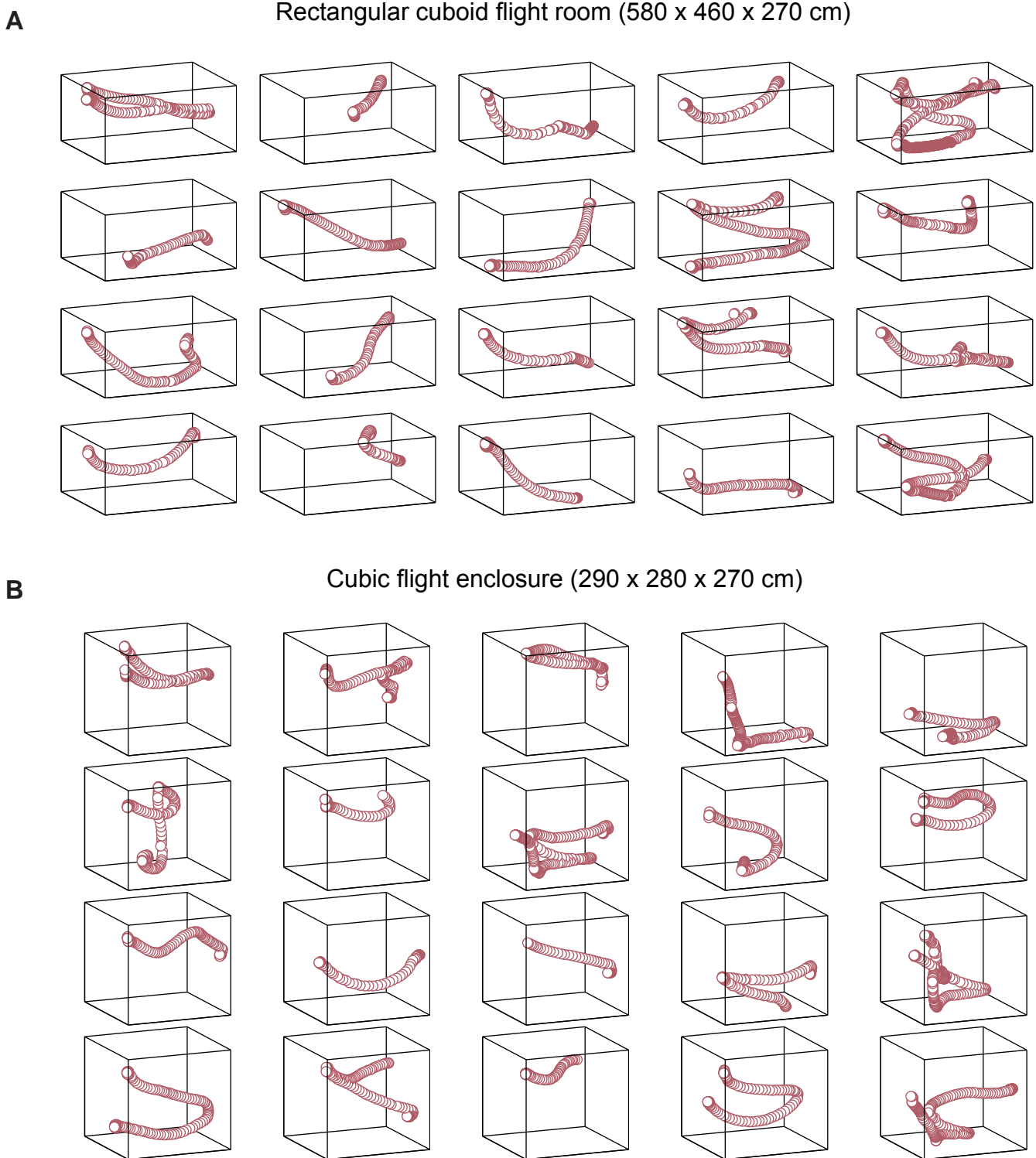**B**   Cubic flight enclosure (290 x 280 x 270 cm)

Fig. S3. Examples of flight trajectories in the two flight setups.
Examples of individual flight trajectories exhibited by bats foraging in the rectangular cuboid flight room (**A**) and the cubic flight enclosure (**B**). The data in (A) and (B) are from two different bats; shown in (A) are 20 example flight trajectories out of a total of 113 flights in a single session, and in (B) are 20 example flights out of a total of 138 flights in a single session. Note the richness and variability of the flight trajectories.

A Crawling box
(2 bats)

B Cubic flight enclosure
(2 bats)

C Rectangular cuboid flight room
(3 bats)
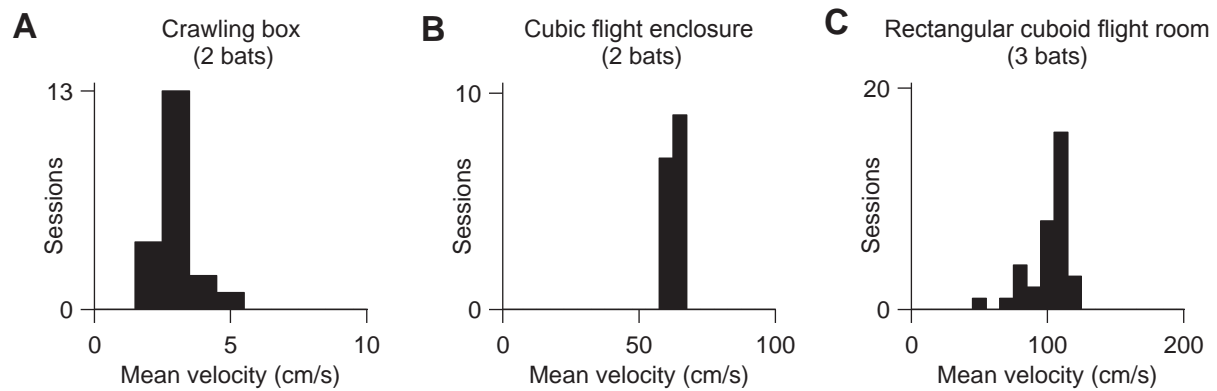
Fig. S4. Movement velocities of bats in different experimental setups.
Distributions of mean movement velocity across three different experimental setups. **(A)** Crawling in a 1.17 x 1.17 m² box (data from ref. *5*). **(B)** Flying in a 2.9 x 2.8 x 2.7 m³ cubic enclosure. **(C)** Flying in a 5.8 x 4.6 x 2.7 m³ rectangular cuboid room. Note that the mean flight velocity was dramatically higher in flight (B and C) compared to crawling (A). Additionally, comparing the two flight setups shows that flight velocity increased substantially with the size of the available environment (compare B versus C); that is, bats flew faster in the larger room. The movement velocities across the 3 different setups spanned almost 2 orders of magnitude.

Supplementary Figure 5 - Page 1

XY projections

Z = 10 cm | Z = 20 | Z = 30 | Z = 40 | Z = 50 | Z = 60 | Z = 70 | Z = 80 | Z = 90

Z = 100 | Z = 110 | Z = 120 | Z = 130 | Z = 140 | Z = 150 | Z = 160 | Z = 170 | Z = 180

Z = 190 | Z = 200 | Z = 210 | Z = 220 | Z = 230 | Z = 240 | Z = 250 | Z = 260 | Z = 270 cm

XZ projections

Y = 10 cm | Y = 20 | Y = 30 | Y = 40 | Y = 50 | Y = 60 | Y = 70 | Y = 80 | Y = 90

Y = 100 | Y = 110 | Y = 120 | Y = 130 | Y = 140 | Y = 150 | Y = 160 | Y = 170 | Y = 180

Y = 190 | Y = 200 | Y = 210 | Y = 220 | Y = 230 | Y = 240 | Y = 250 | Y = 260 | Y = 270

Y = 280 | Y = 290 | Y = 300 | Y = 310 | Y = 320 | Y = 330 | Y = 340 | Y = 350 | Y = 360

Y = 370 | Y = 380 | Y = 390 | Y = 400 | Y = 410 | Y = 420 | Y = 430 | Y = 440 | Y = 450

Y = 460 cm
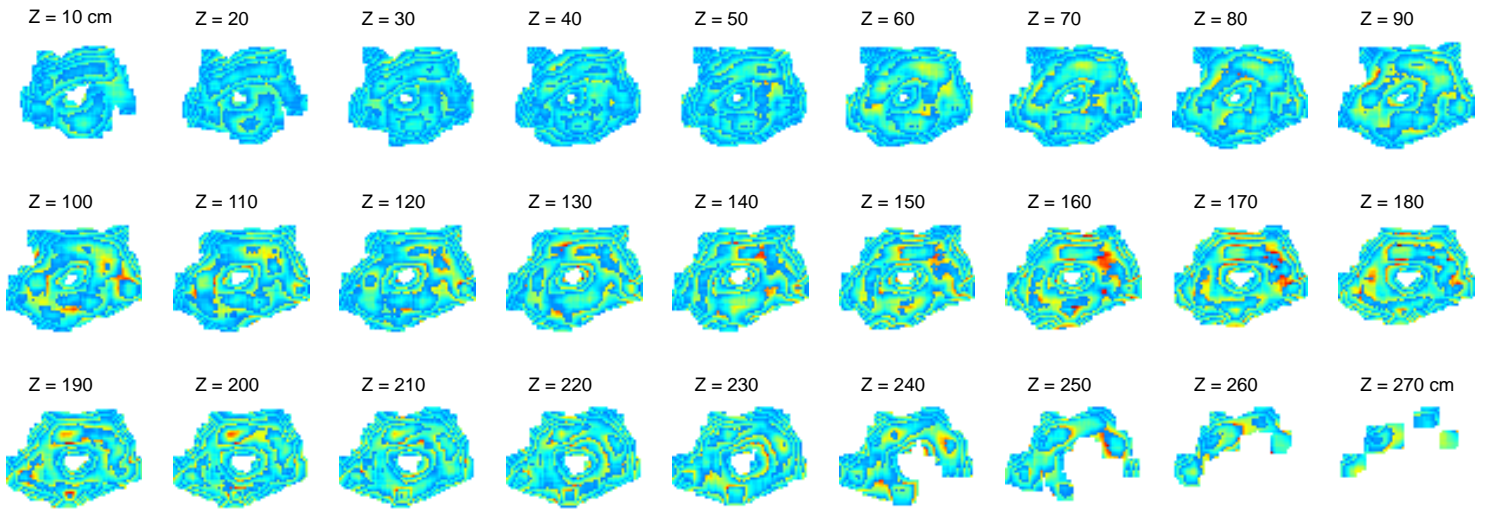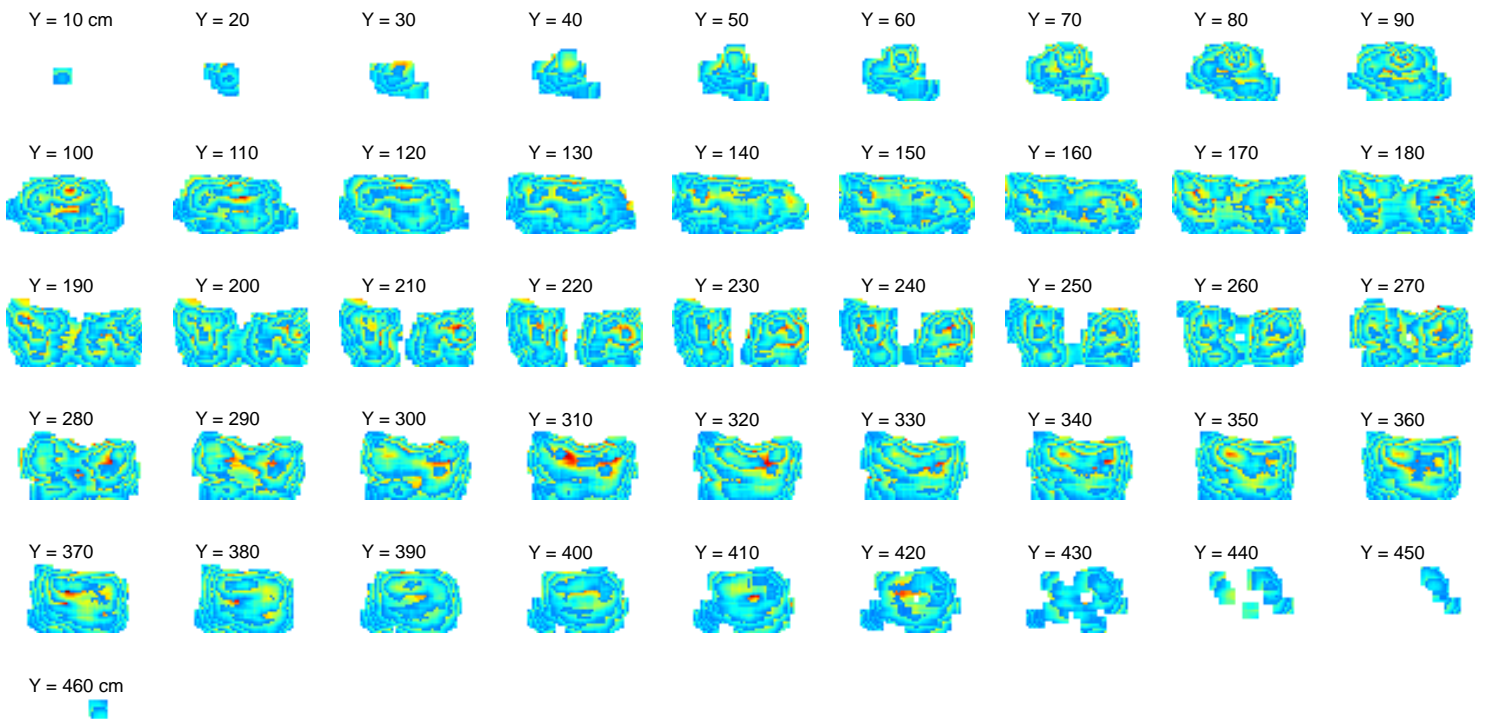
YZ projections
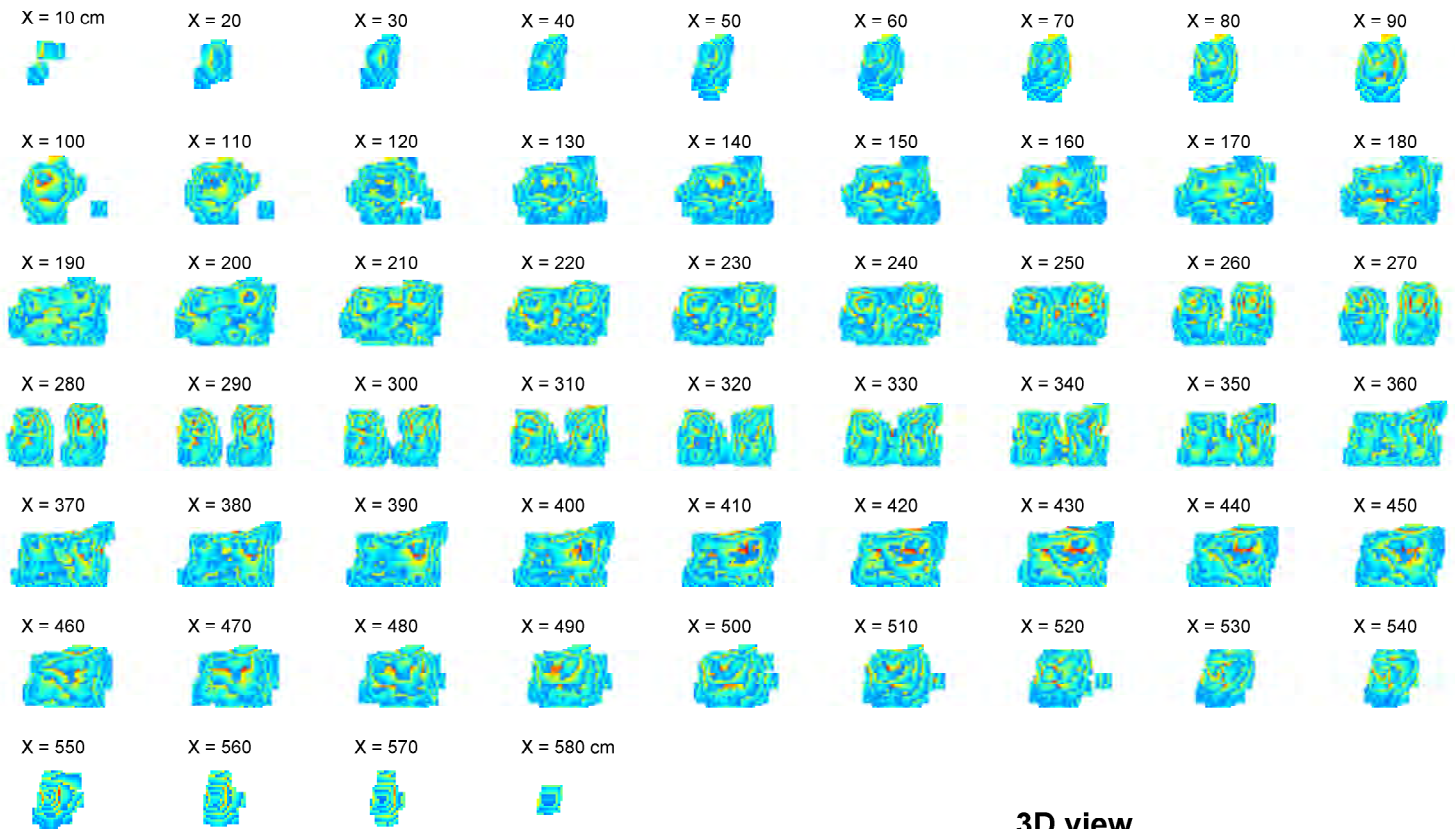
3D view
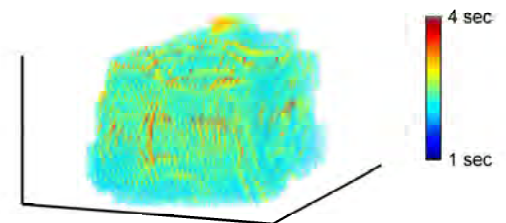
Fig. S5. Spatial distribution of the time spent by a bat in different 3D voxels during flight in the rectangular-cuboid flight room. Example of the distribution of flight-times spent by the bat in different locations across the flight room, during a single behavioral session. Data are shown in color-coded 2D slice representation (10-cm slice thickness) for all three projections of the flight room. Page 1: XY and XZ projections. Page 2: YZ projections, as well as a depiction of the full 3D coverage. All panels are color-coded using the same color scale (see color bar on bottom right); colors range from dark blue (1 sec) to red (4 sec; the time-spent values actually reached up to 4.16 sec, but were clipped here at 4 sec for display purposes, to allow direct comparison with the data for the cubic flight enclosure, shown in fig. S6; see also (*19*)). Note that the volume of this large flight-room (580 x 460 x 270 cm³) was covered relatively uniformly by the bat during the behavioral session.

Supplementary Figure 6 - Page 1

XY projections

Z = 10 cm   Z = 20   Z = 30   Z = 40   Z = 50   Z = 60   Z = 70   Z = 80   Z = 90

Z = 100   Z = 110   Z = 120   Z = 130   Z = 140   Z = 150   Z = 160   Z = 170   Z = 180

Z = 190   Z = 200   Z = 210   Z = 220   Z = 230   Z = 240   Z = 250   Z = 260   Z = 270 cm

XZ projections

Y = 10 cm   Y = 20   Y = 30   Y = 40   Y = 50   Y = 60   Y = 70   Y = 80   Y = 90

Y = 100   Y = 110   Y = 120   Y = 130   Y = 140   Y = 150   Y = 160   Y = 170   Y = 180

Y = 190   Y = 200   Y = 210   Y = 220   Y = 230   Y = 240   Y = 250   Y = 260   Y = 270

Y = 280 cm
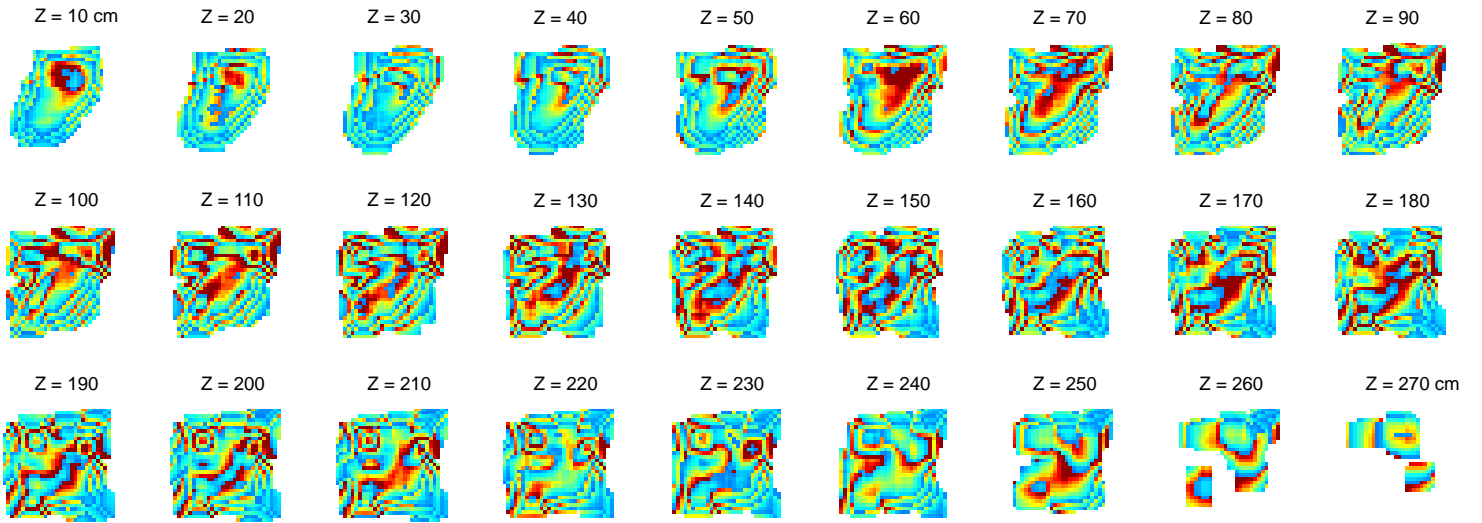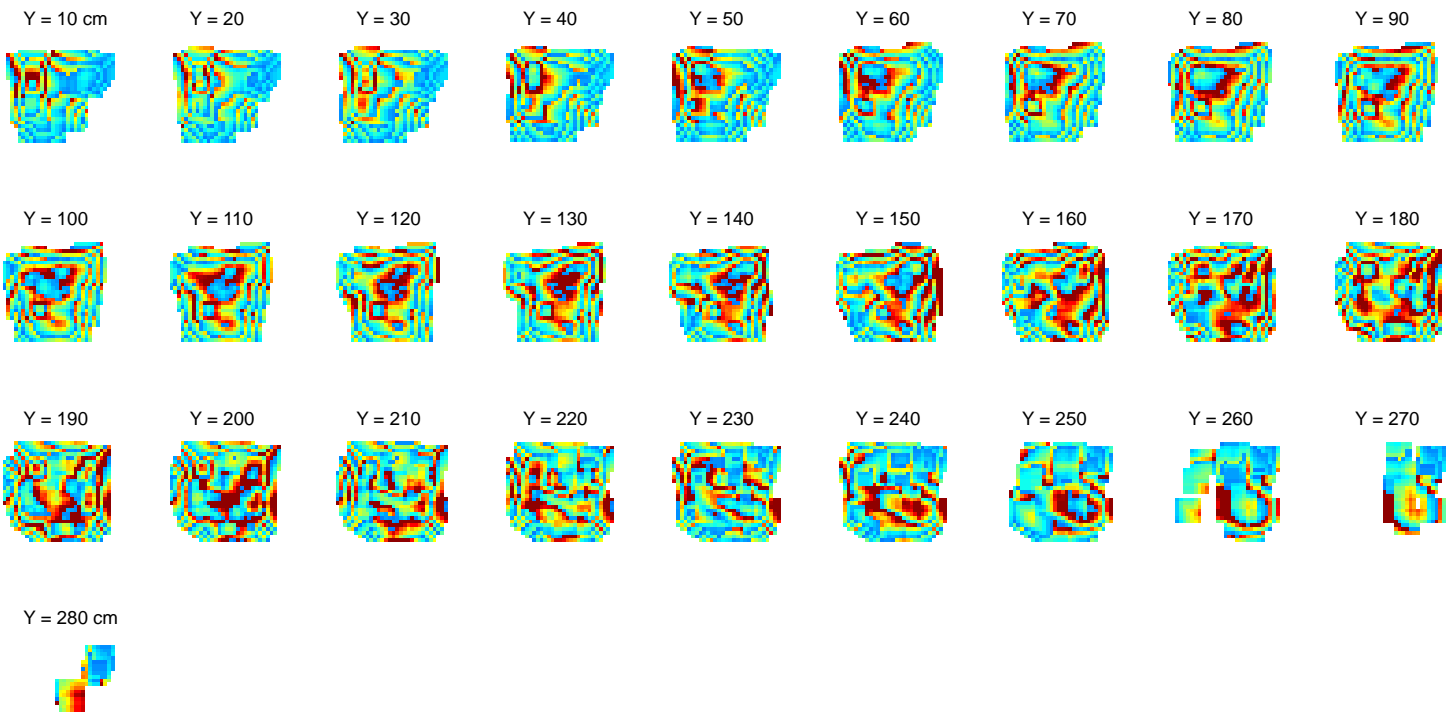
YZ projections
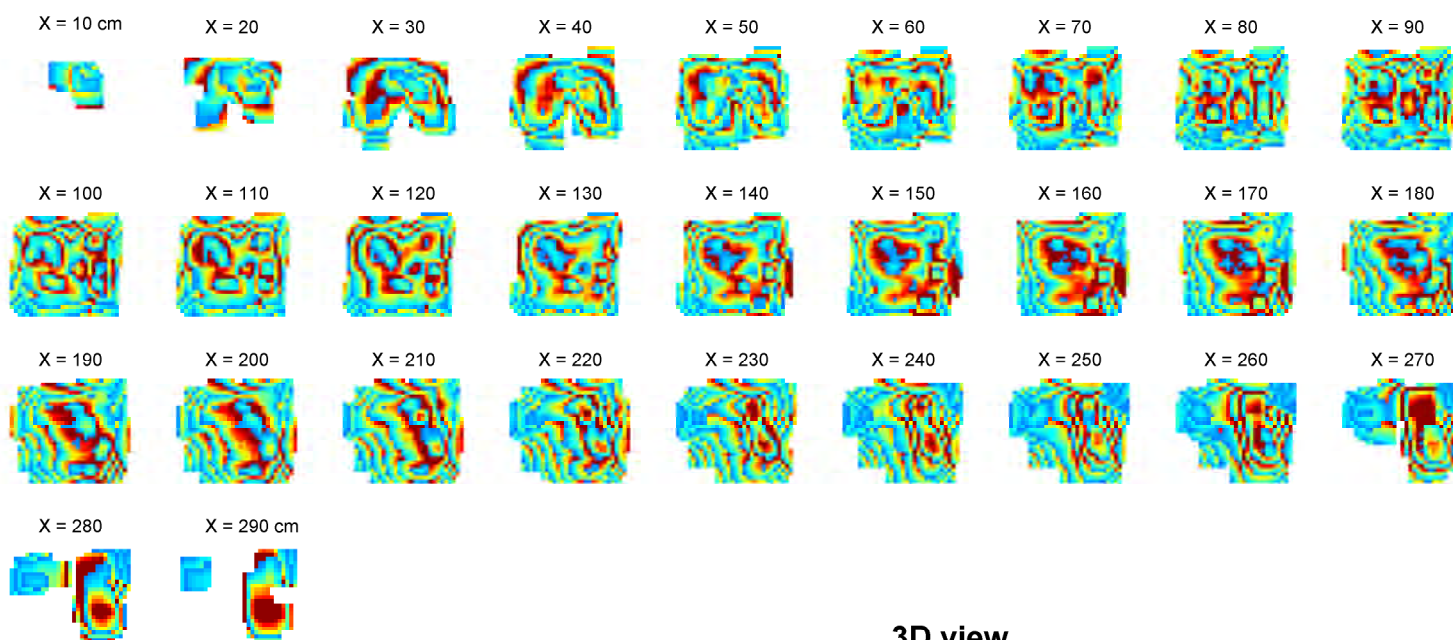
3D view
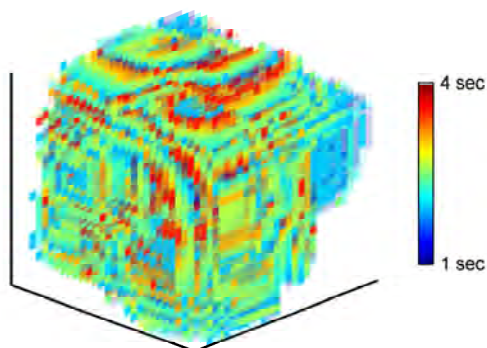
Fig. S6. Spatial distribution of the time spent by a bat in different 3D voxels during flight in the cubic enclosure.
Example of the distribution of flight-times spent by the bat in different locations across the cubic flight enclosure, during a single behavioral session. Data are from the same day as the example place-cell shown in fig. S15. Data shown in color-coded 2D slice representation (10-cm slice thickness) for all three projections of the flight room. Page 1: XY and XZ projections. Page 2: YZ projection, as well as a depiction of the full 3D representation. All panels are color-coded using the same color scale (see color bar on bottom right); colors range from dark blue (1 seconds) to red (4 sec; the time-spent values actually reached up to 9.68 sec, but were clipped here at 4 sec for display purposes, to allow direct comparison with the data for the rectangular cuboid flight room, shown in fig. S5; see also (*19*)). Note that the volume of this cubic enclosure (290 x 280 x 270 cm^3) was covered relatively uniformly by the bat during the behavioral session. Also note that in the cubic flight enclosure there was even denser coverage (larger time-spent per voxel) than in the rectangular cuboid flight room, due to the smaller volume of the cubic enclosure (compare this figure to fig. S5 - both figures have the same color-scale).

A

B

C

Wired | Wireless: Antenna 1 | Wireless: Antenna 2

Location # 1

Location # 2

Location # 3

Energy 3 / Energy 1 (axes)
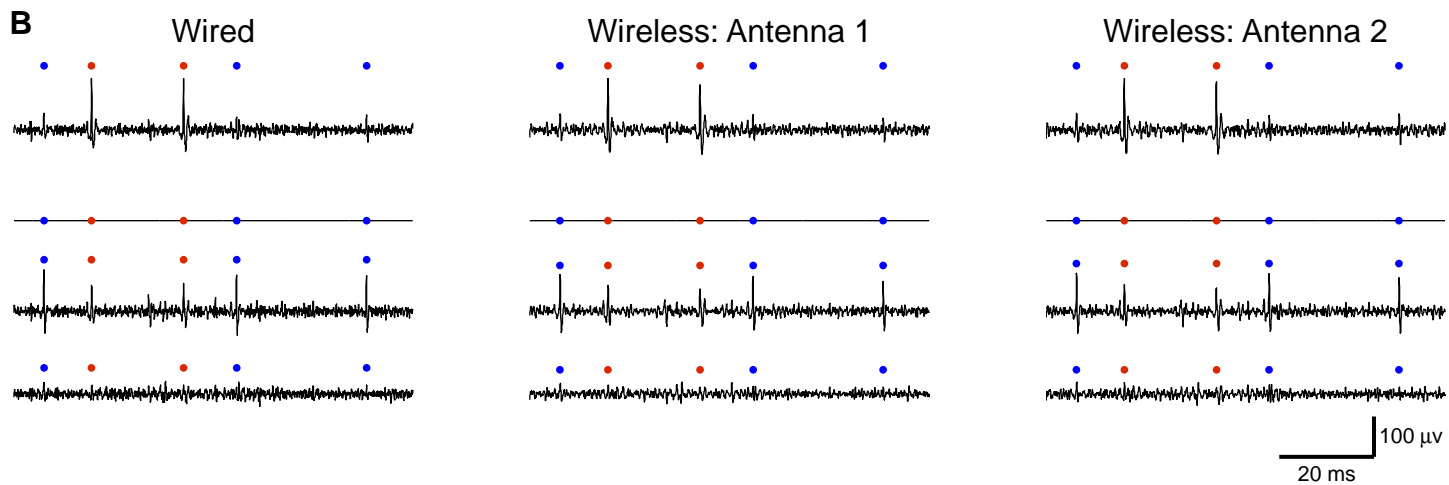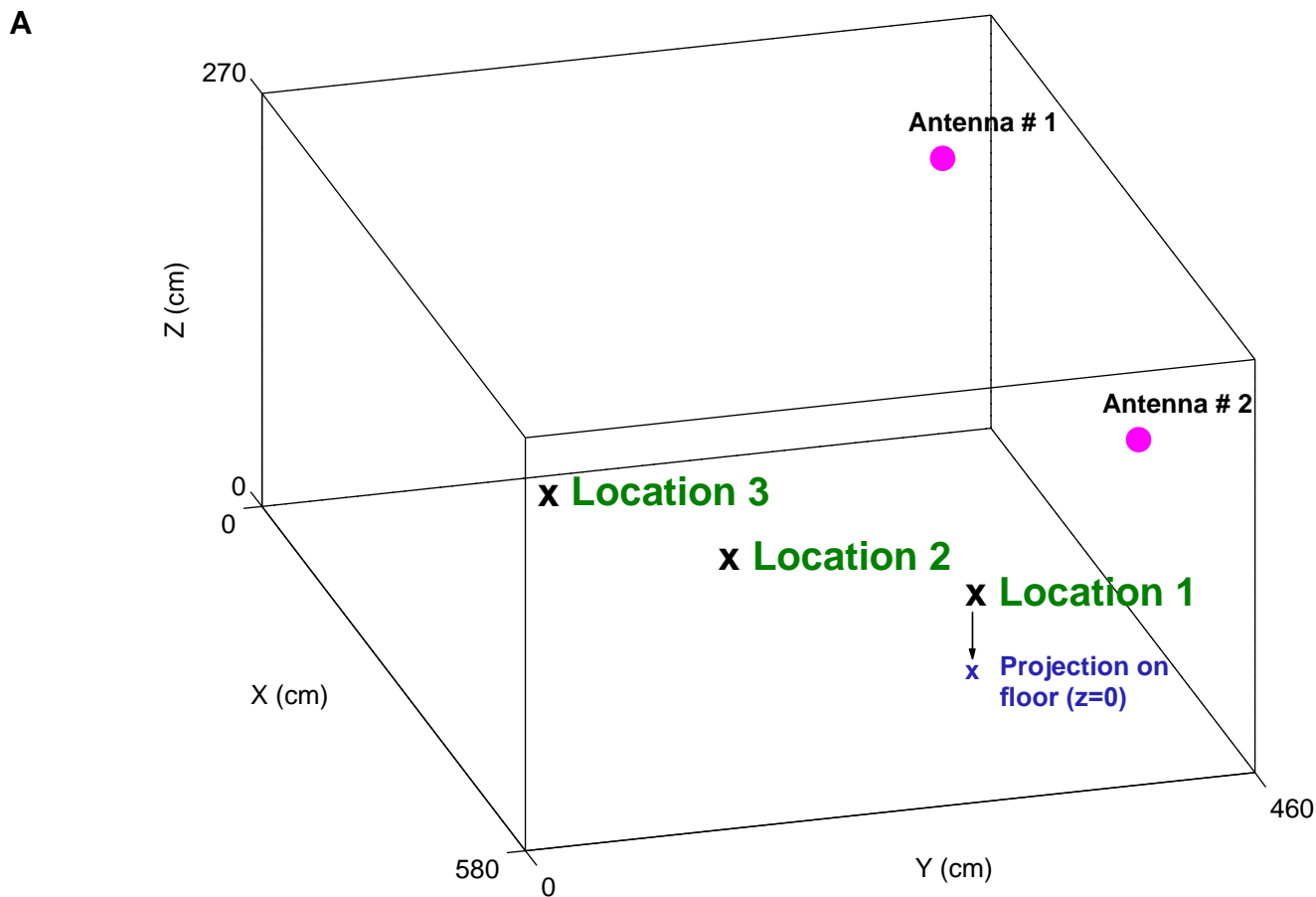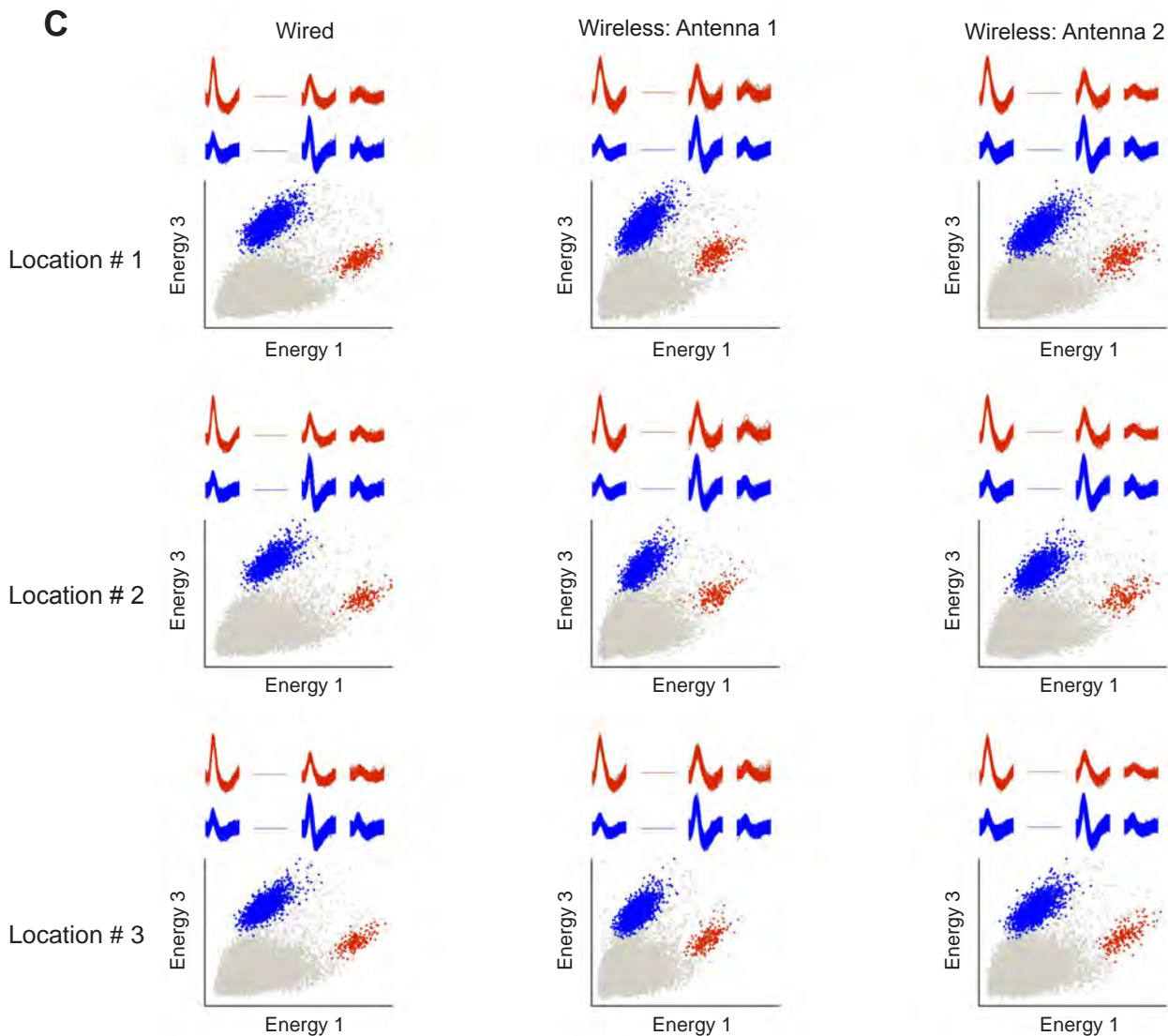
Fig. S7. Simultaneous wired and wireless recordings in bats demonstrate the good quality of the wirelessly transmitted signal. Simultaneous wired (tethered) and wireless neural recordings were conducted in a stationary bat, positioned on a pedestal at a height of 51 cm above the floor, from a single tetrode in the bat hippocampal CA1 region. (**A**) Recording locations in the room (green) and positions of the two receiving antennas of the neural-telemetry system (pink dots). In blue is an example of the projection of location 1 onto the floor, z = 0. (**B**) Example of a neural trace recorded on the wired (left column) and wireless system (middle and right columns); recorded in 'location 3' in the flight room. Red and blue markers above neural trace correspond to the red and blue clusters in panel (C). Note that channel 2 of the recording tetrode was disconnected. Scale bars, 20 ms, 100 μV. The telemetry system had 4 channels, which allowed transmitting the signal from only one recording tetrode; the identity of the transmitted tetrode could be set by dedicated jumper-wires, and the "best tetrode" was chosen daily prior to the recording by connecting the bat to a regular wired system and choosing the tetrode with the best-quality spikes (*19*). (**C**) Spike-waveforms and two-dimensional projections of spike energies of recorded CA1 neurons are shown before transmission (left column, wired recording) and after transmission (middle and right columns, wireless system), for the 3 recording locations in the room.
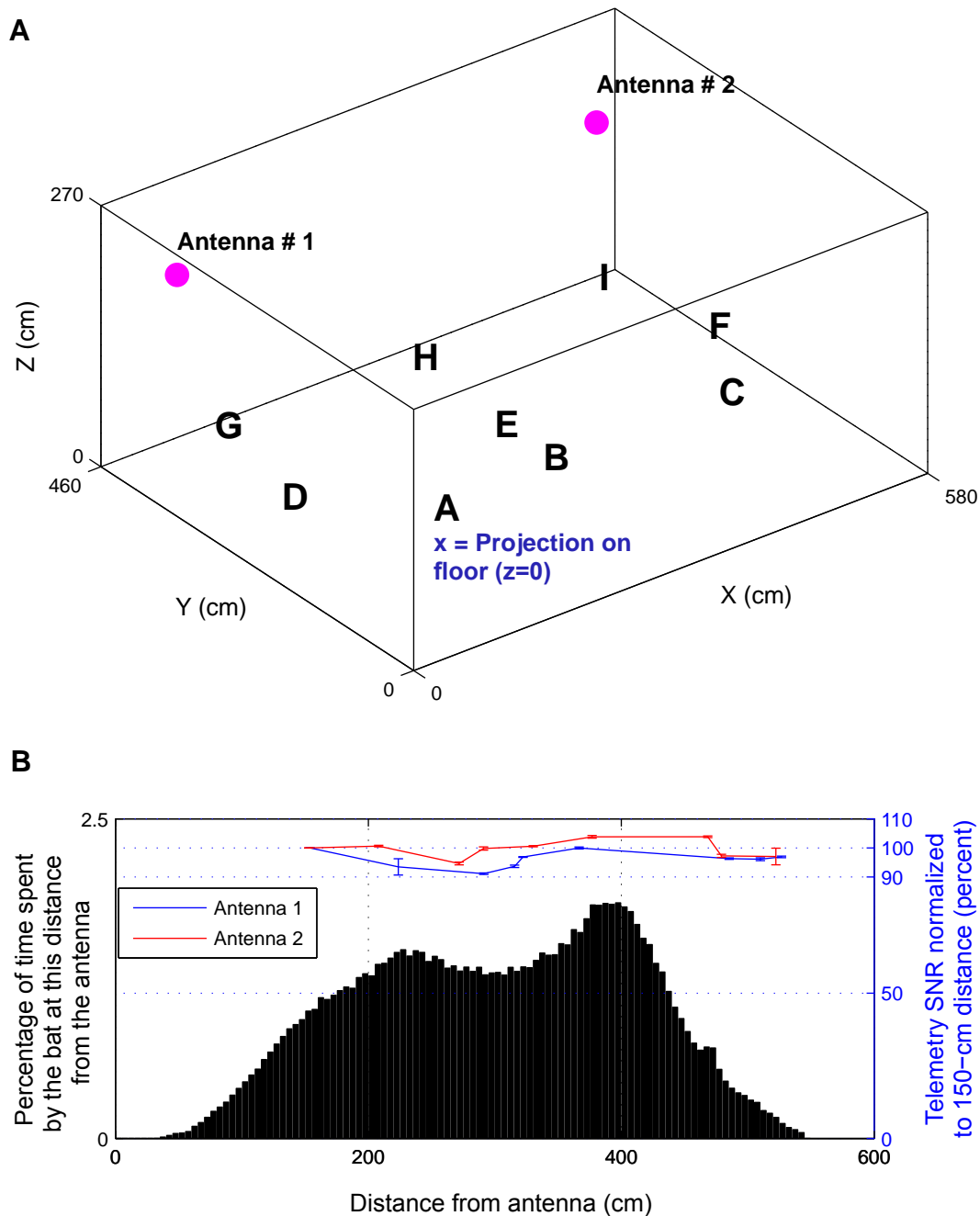
Supplementary Figure 8

Fig. S8. Signal quality of the wireless neural-telemetry system is stable with increasing distance from the antennas, throughout the flight room. (**A**) A synthetic signal (280-μV sine wave at 1 kHz) was recorded in 9 locations in the flight room (locations A-I) at a height of 51-cm above the floor (blue 'x', projection of location A onto the floor: z = 0); the 9 locations varied in their distances from the two antennas (pink dots). (**B**) The signal-to-noise ratio (SNR) of the telemetry system was computed for each recording location as the ratio between the spectral power around 1 kHz (999.5 – 1000.5 Hz) and the spectral power outside that range. Blue and red lines: SNR did not change with increasing distance from the antenna; the SNR was computed for all locations and for each antenna (blue and red curves, mean ± s.e.m, right y-axis). Black histogram: distribution of all visited locations over all bats and all behavioral sessions, as collected during neural recordings in the rectangular-cuboid flight setup, plotted as a function of the distance from both antennas. Note that the SNR of the telemetry system (blue and red curves) was very stable with distance, across all the behaviorally-relevant locations of bats in the flight-room (black histogram; note the stability of the red and blue curves throughout the entire x-extent of the black histogram).
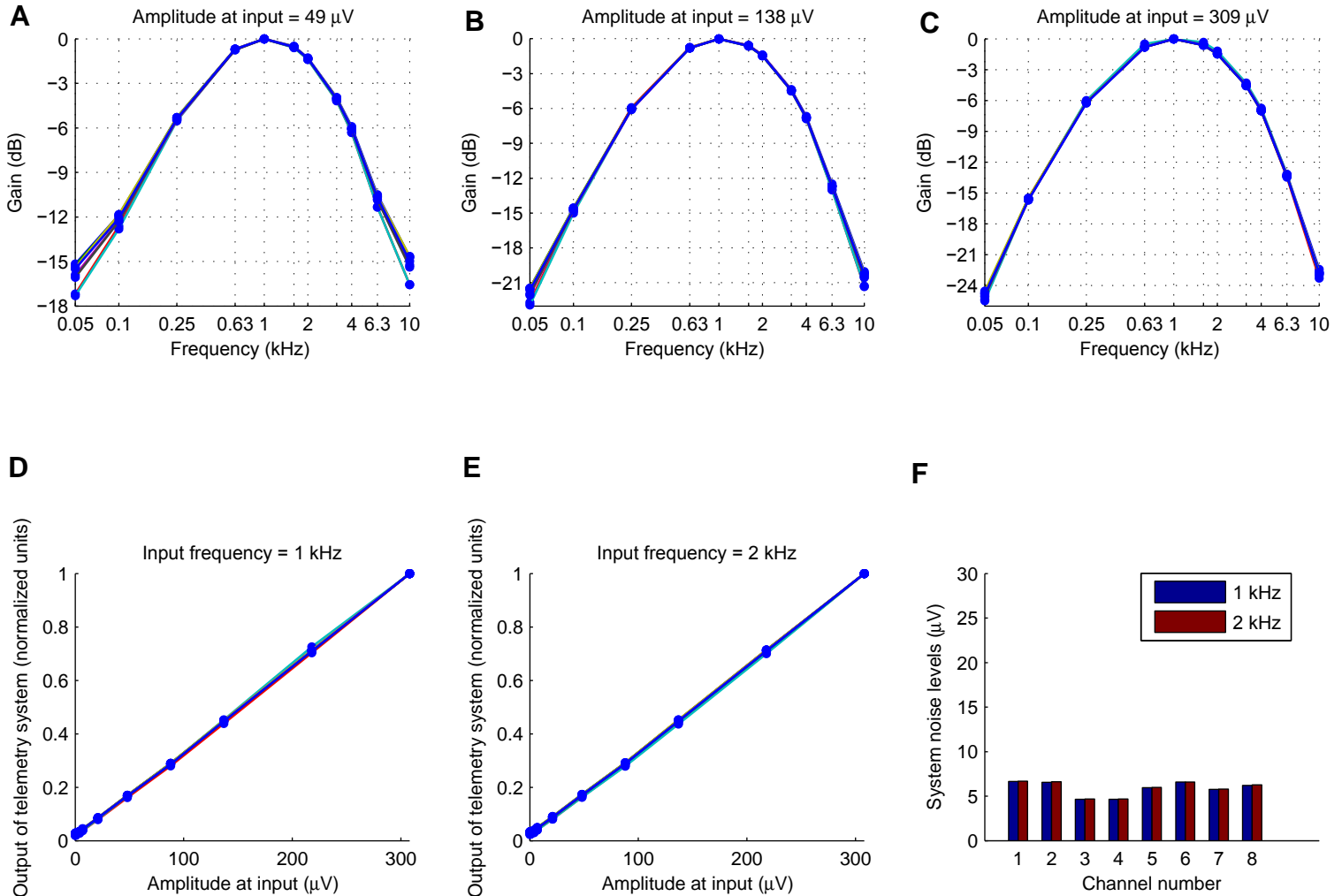
Fig. S9. Frequency characteristics, linearity, and low system-noise of the wireless neural-telemetry system. Measured by inputting pure sine waves into the system. (**A** to **C**), Frequency response of the wireless telemetry system is shown for the 8 channels (8 different colors, 4 recording channels x 2 antennas per channel), plotted for different input-signal amplitudes (zero-to-peak input amplitudes are: (A) 49 µV ; (B) 138 µV ; (C) 309 µV). Note the high bandwidth, which allowed high-fidelity recordings of action potentials (–6 dB bandwidth, ~250 Hz to 4 kHz; –12 dB bandwidth, ~100 Hz to 6.3 kHz). (**D** to **E**) Amplitude responses for the 8 channels are shown for a 1-kHz input signal (D) and 2-kHz input (E). Note the highly linear response for all recording channels from 0 µV until 309 µV (zero-to-peak), covering the range of typical action-potential amplitudes. Above 309 µV the system looses its linearity (not shown), but this was seldom a problem as we rarely had spikes larger than 300 µV (zero-to-peak). (**F**) Telemetry system noise measured for a very weak, 0.1-µV sine-wave input at 1 kHz (blue) and 2 kHz (red). Usage of near-zero input allowed estimating here the telemetry system internal noise. Note that the system noise was very low, ranging between 4 – 7 µV; on all recording channels the system noise was < 7 µV.

Supplementary Figure 10
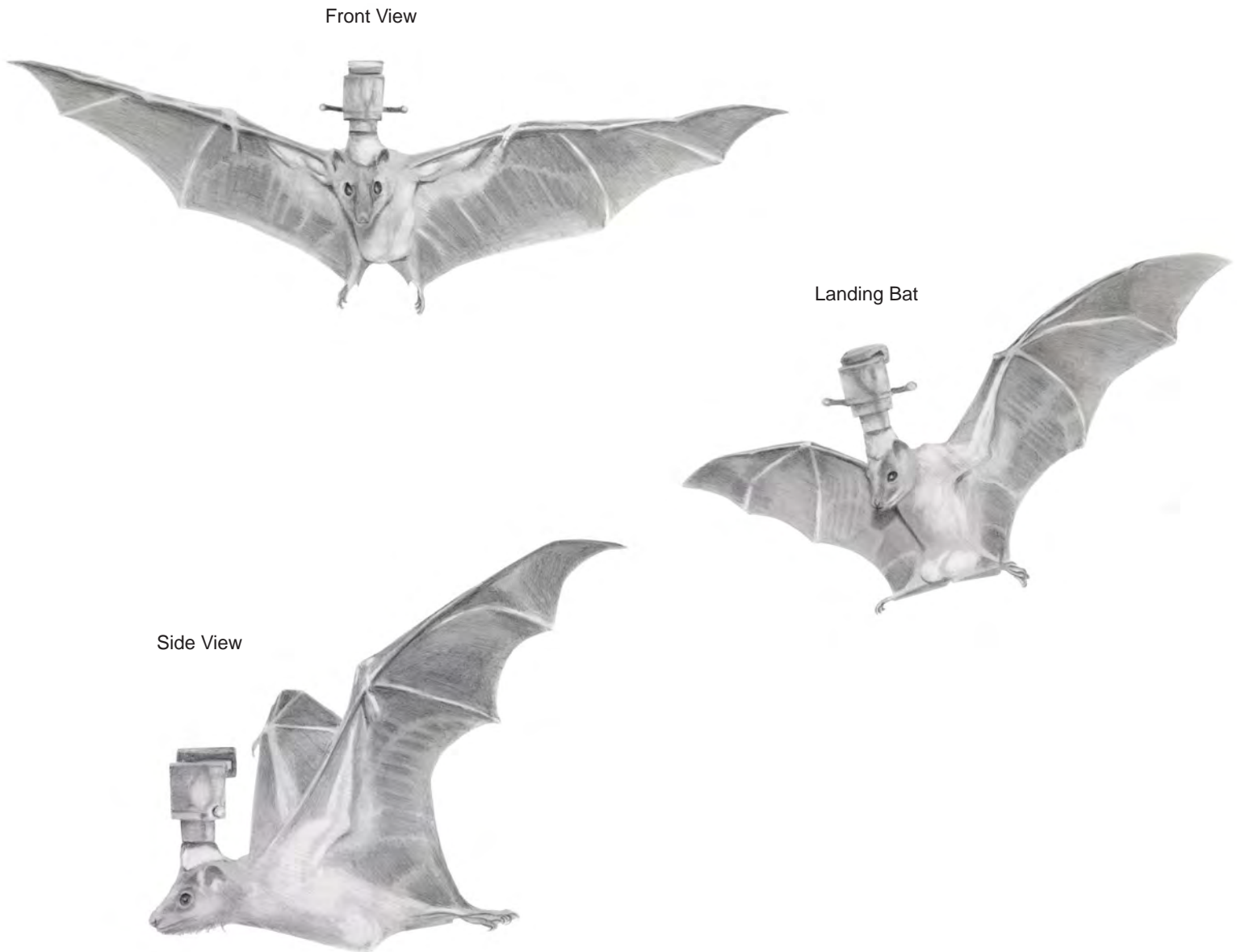
Front View

Landing Bat

Side View

Fig. S10. Illustration of telemetry system on the head of a flying bat, drawn to scale.
Drawings by Sharon Kaufman. Note that the combined weight of the wireless system – including the headstage, amplifier, wireless transmitter, battery and plastic casing – was 12 gr. Together with the 2-gr microdrive, the total net weight on the bat's head was 14 gr. The average weight of Egyptian fruit bats used for this study was 172 gr, hence the full telemetry system comprised ~8% of the bat's weight. In comparison, we showed in the past that these bats can carry a 13-gr weight of a miniaturized GPS, and fly almost 100 km with it, in the wild (29); moreover, females in the wild, weighing less than the males used in this study, fly with pups on them that can weigh up to ~50 gr (N.U., personal observations), which is 4 times heavier than our telemetry system. Thus, the weight of our telemetry system is not very large compared to the carrying capabilities of this bat species.
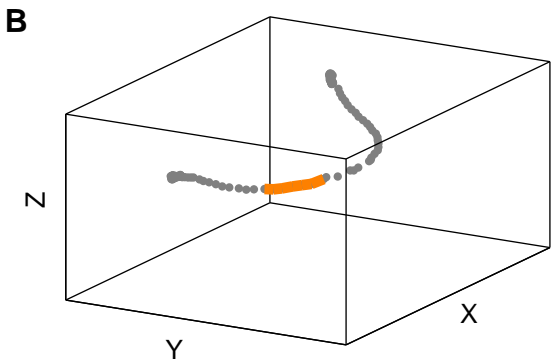
A

Spikes | Spikes | Artifacts | Spikes | Artifacts

50 μv
5 ms

50 μv
5 ms

50 μv
1 ms

50 μv
5 ms

50 μv
1 ms

100 μv

50 ms

B

Z

Y

X

C

Velocity (m/s)

1.3

0.6

0

Vx
Vy
Vz
Vtotal

690   692   694   696

Time (s)

D

% of excluded recording
time due to artifacts
during flight

10

8

6

4

2

0

6.4

4

2.4

0.11

0

0.051

1−3   4−6   7−9   10−12   13−15   16−17
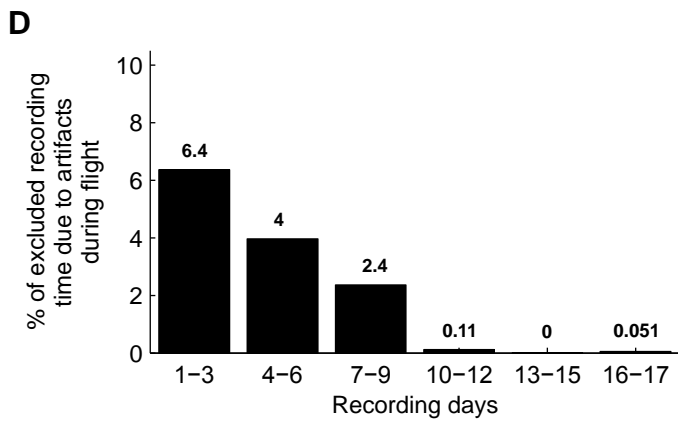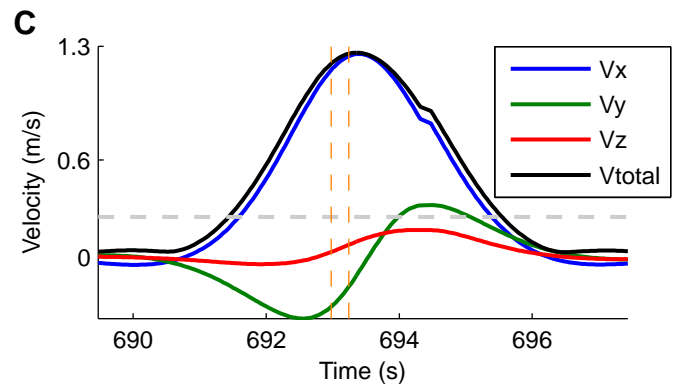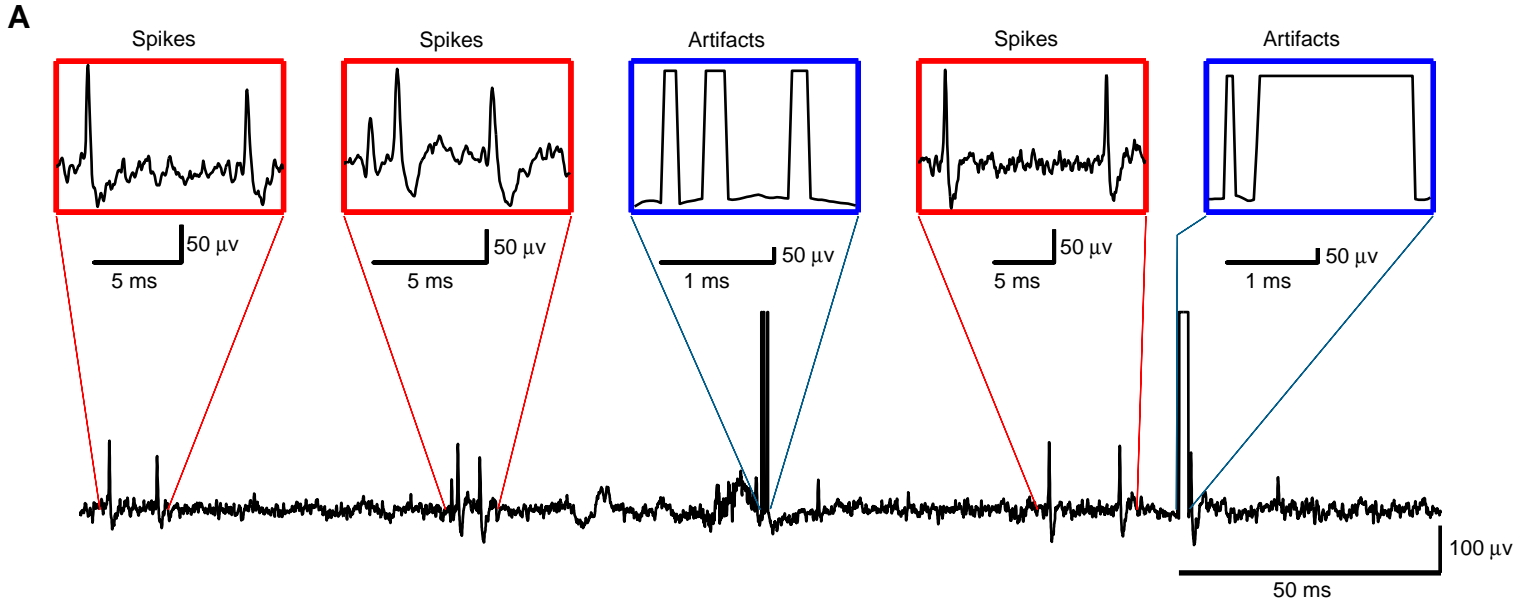
Recording days

Fig. S11.   Wing-beat recording artifacts in freely flying bats are easily identifiable and go down over recording days.   (**A**) Shown is a representative neural trace recorded from bat hippocampal area CA1 during free flight, using the wireless neural-telemetry system. Data are from the 5th recording day post-surgery. Top: Zoom-in on action potentials ('Spikes', red boxes) and wing-beat artifacts ('Artifacts', blue boxes). Horizontal and vertical scale bars are indicated. Note that wing-beat artifacts have large amplitude and a characteristic rectangular shape that makes it easy to differentiate them from spikes. Note also that the artifacts are short-duration, transient events that do not obscure the detection of spikes throughout the majority of the recording.   (**B**) The flight segment (gray) during which the neural trace in (A) was recorded (the time-epoch shown in A is highlighted in orange).   (**C**) Velocity dynamics of this flight. Shown are the velocities in all the three major axes during flight (Vx,Vy,Vz) as well as the overall velocity (Vtotal). Vertical dashed lines (orange color) correspond to the time-segment of the neural trace shown in (A) and to the flight segment shown in orange in (B). Horizontal dashed line (gray color) correspond to the velocity threshold used for the detection of flight epochs (25 cm/s; see (*19*)). (**D**) Fraction of artifact time out of the total flight time, plotted as function of recording days. Data pooled and averaged across all five bats in both of the flight setups (rectangular cuboid room and cubic flight enclosure) (*19*); the value for each bin is also indicated. Note that the wing-beat artifacts comprised only a small fraction of the total flight time (3.6 ± 0.91% on average), and this fraction steadily decreased across recording days (presumably because bats learned not to hit the microdrive with their wings, as this was not convenient for the bats).
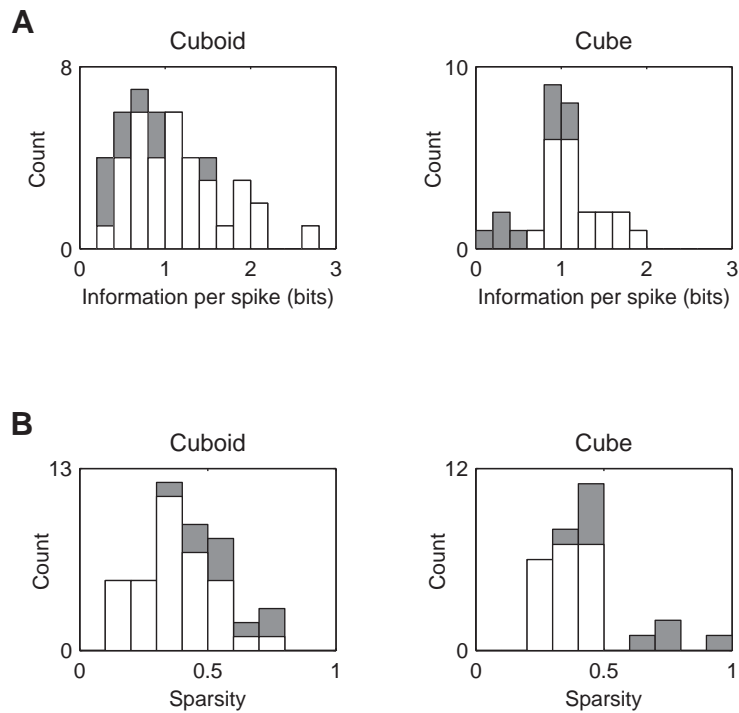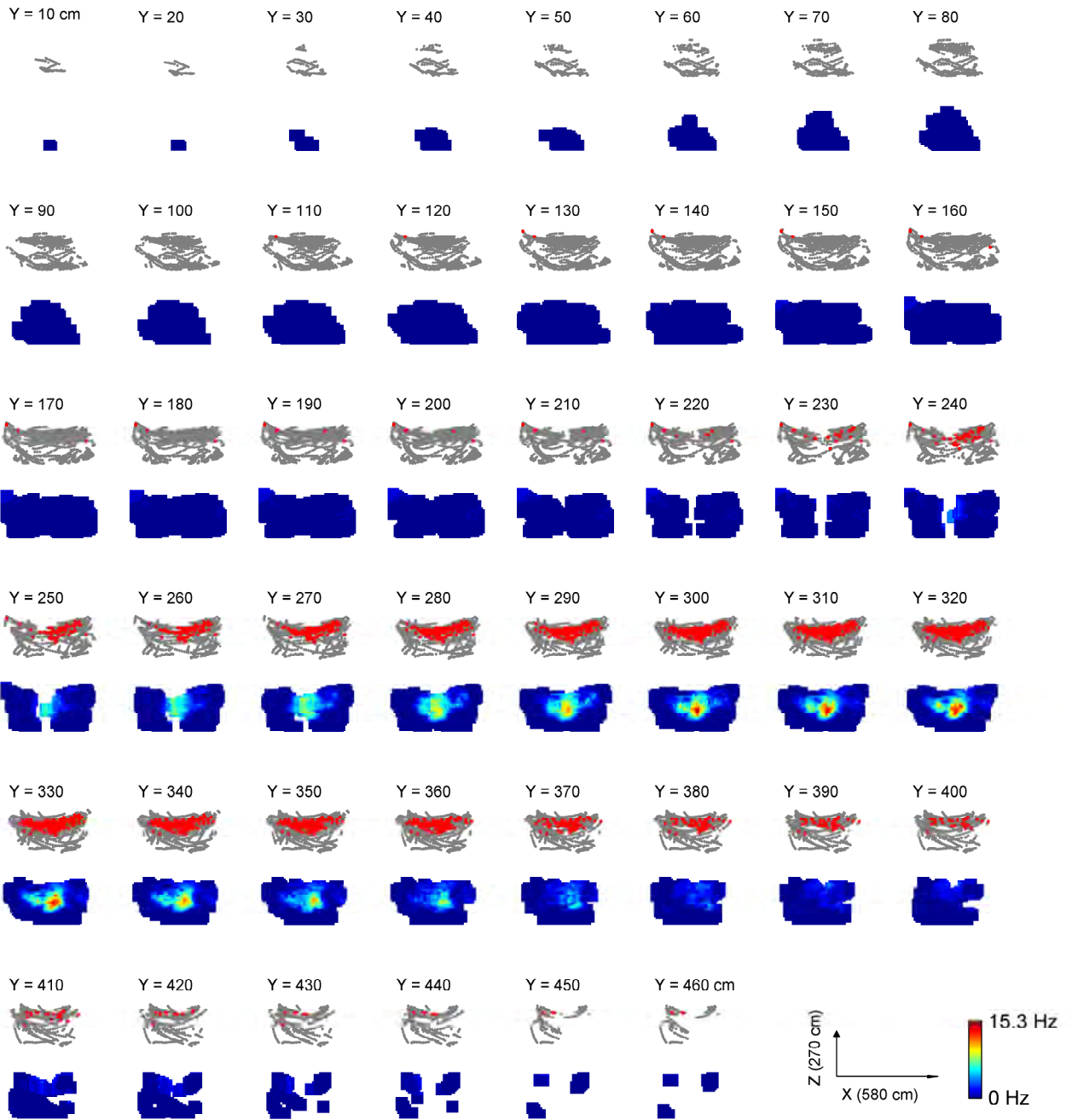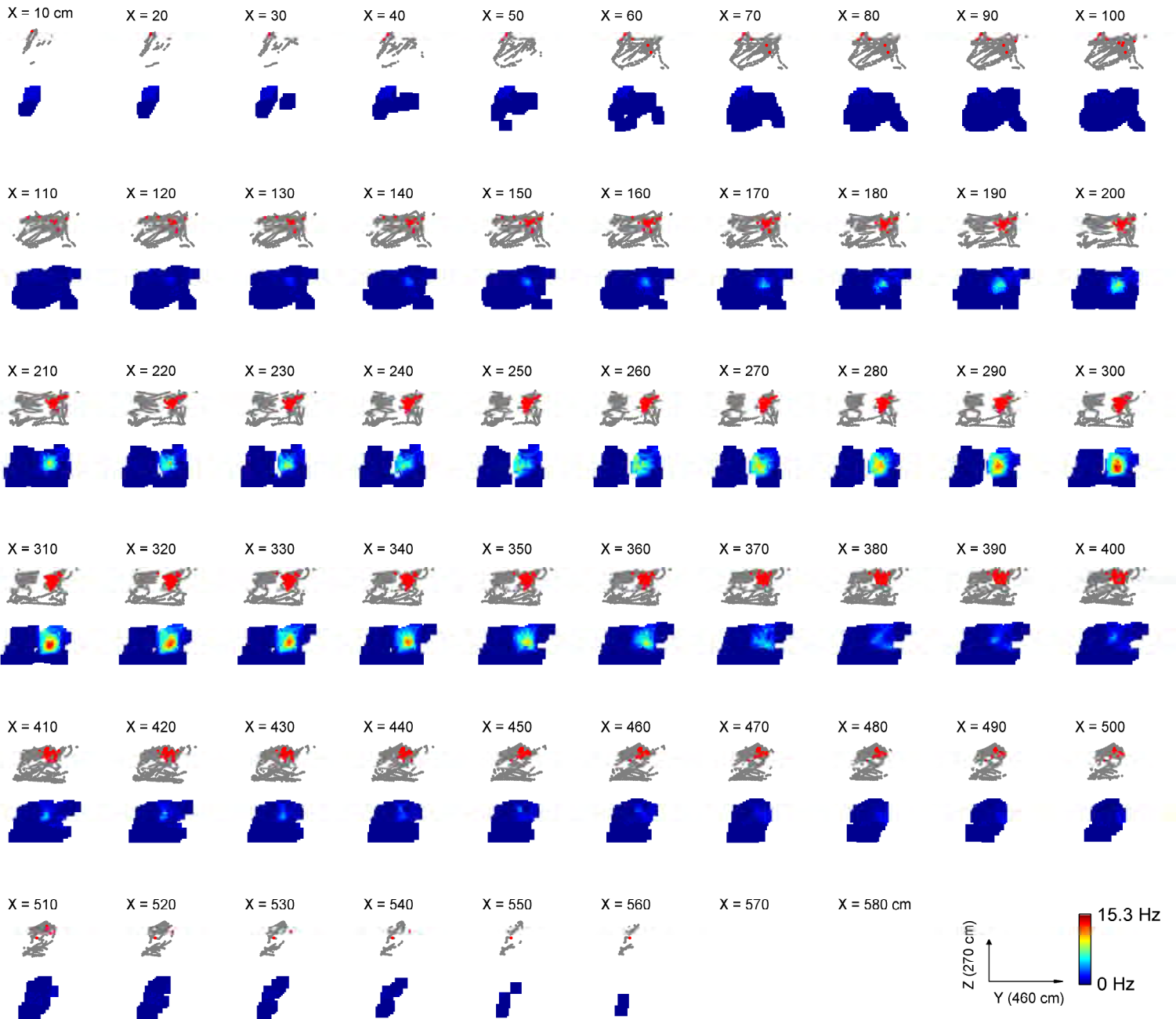
Fig. S12. Distributions of spatial-information and sparsity.
(A and **B**) Distributions of two indices, spatial-information per spike (A) and sparsity (B), for all the active hippocampal CA1 neurons recorded in freely-flying bats in either the rectangular-cuboid flight room (left, n = 44 cells) or in the cubic flight enclosure (right, n = 29 cells). White bars, neurons that were classified as place-cells, based on the shuffling procedure (*19*); gray bars, neurons not classified as place-cells.

Supplementary Figure 13 - Page 1 (XZ projections)

Y = 10 cm Y = 20 Y = 30 Y = 40 Y = 50 Y = 60 Y = 70 Y = 80

Y = 90 Y = 100 Y = 110 Y = 120 Y = 130 Y = 140 Y = 150 Y = 160

Y = 170 Y = 180 Y = 190 Y = 200 Y = 210 Y = 220 Y = 230 Y = 240

Y = 250 Y = 260 Y = 270 Y = 280 Y = 290 Y = 300 Y = 310 Y = 320

Y = 330 Y = 340 Y = 350 Y = 360 Y = 370 Y = 380 Y = 390 Y = 400

Y = 410 Y = 420 Y = 430 Y = 440 Y = 450 Y = 460 cm

Z (270 cm)
X (580 cm)

15.3 Hz

0 Hz

Supplementary Figure 13 - Page 2 (YZ projections)

X = 10 cm   X = 20   X = 30   X = 40   X = 50   X = 60   X = 70   X = 80   X = 90   X = 100

X = 110   X = 120   X = 130   X = 140   X = 150   X = 160   X = 170   X = 180   X = 190   X = 200

X = 210   X = 220   X = 230   X = 240   X = 250   X = 260   X = 270   X = 280   X = 290   X = 300

X = 310   X = 320   X = 330   X = 340   X = 350   X = 360   X = 370   X = 380   X = 390   X = 400

X = 410   X = 420   X = 430   X = 440   X = 450   X = 460   X = 470   X = 480   X = 490   X = 500

X = 510   X = 520   X = 530   X = 540   X = 550   X = 560   X = 570   X = 580 cm

Z (270 cm)
Y (460 cm)

15.3 Hz

0 Hz
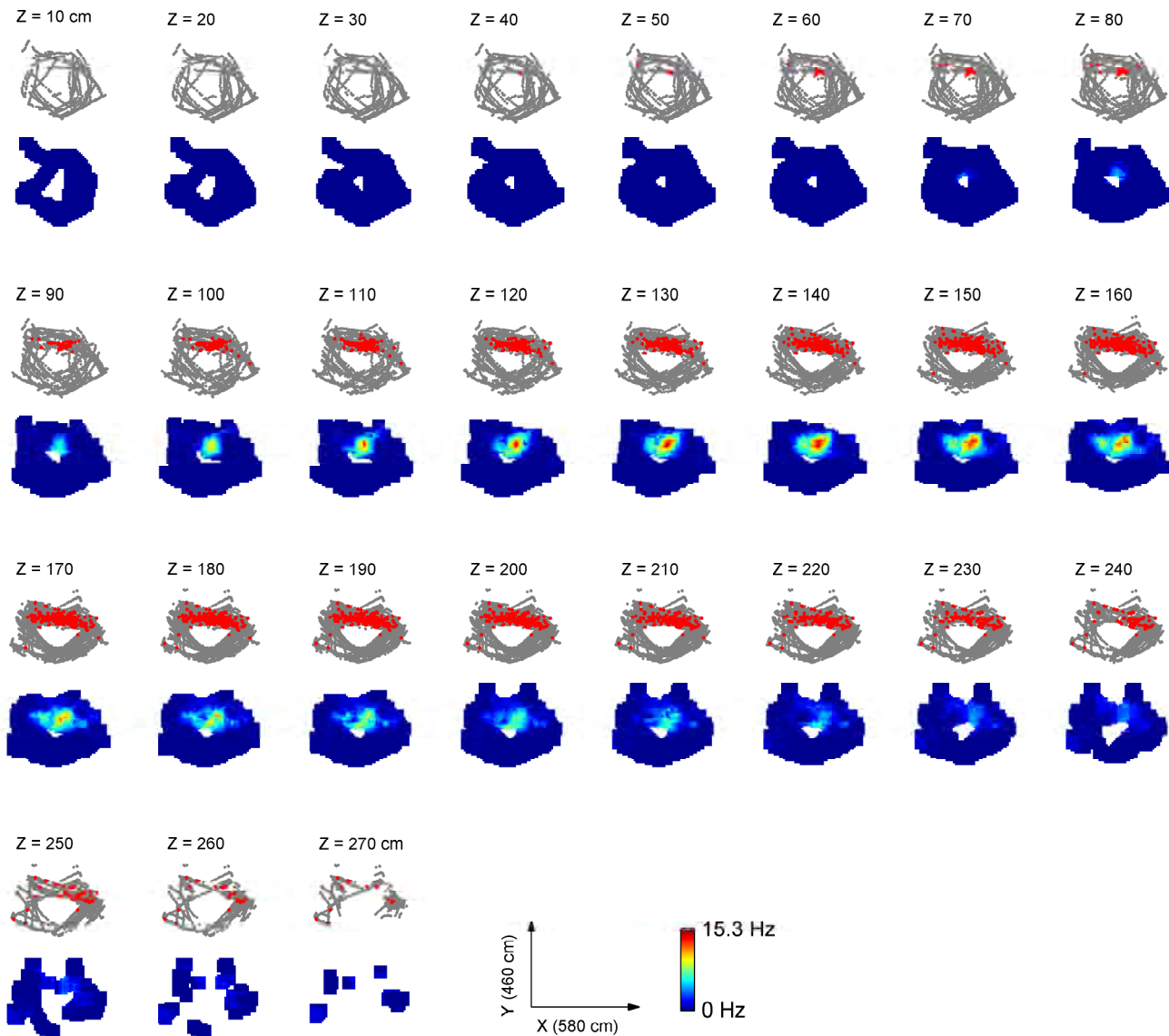
Fig. S13. 2D slice cuts through a 3D place field. Raw data (top) and color-coded rate maps (bottom) of the example cell shown in Fig. 2 of the main text, plotted here as sequential 2D slice cuts through the 3D rate-map (10-cm slice thickness). Page 1, slices in the XZ plane ; Page 2, YZ plane ; Page 3, XY plane. Bottom right on each page: Spatial scale bars and firing-rate color scale. The same spike (red dot) may repeat across several successive slices, because adaptive voxel size was larger than 10 x 10 x 10 cm^3 (*19*).
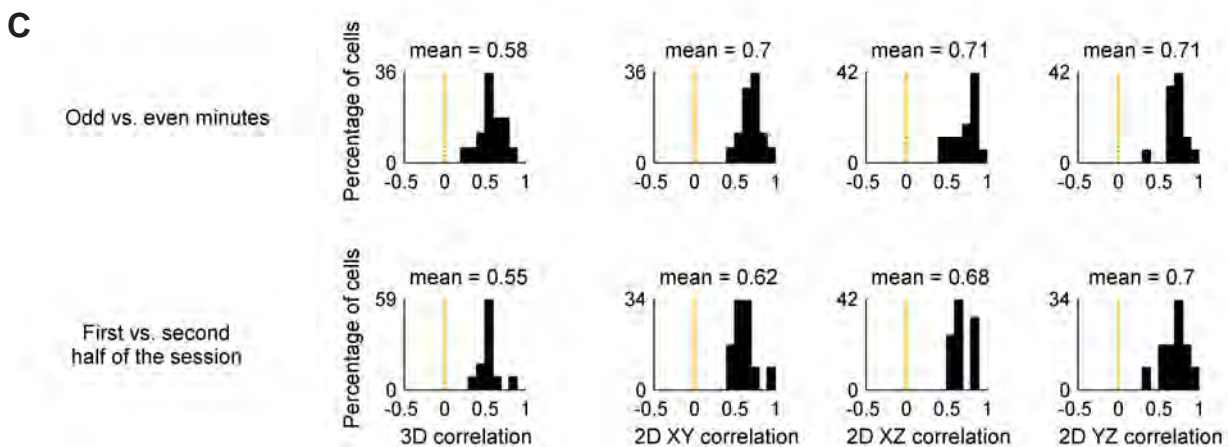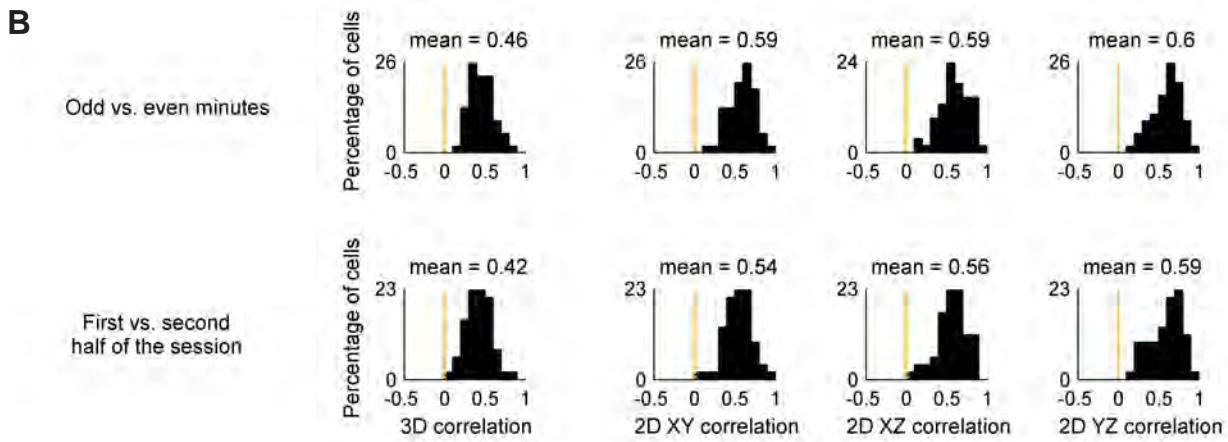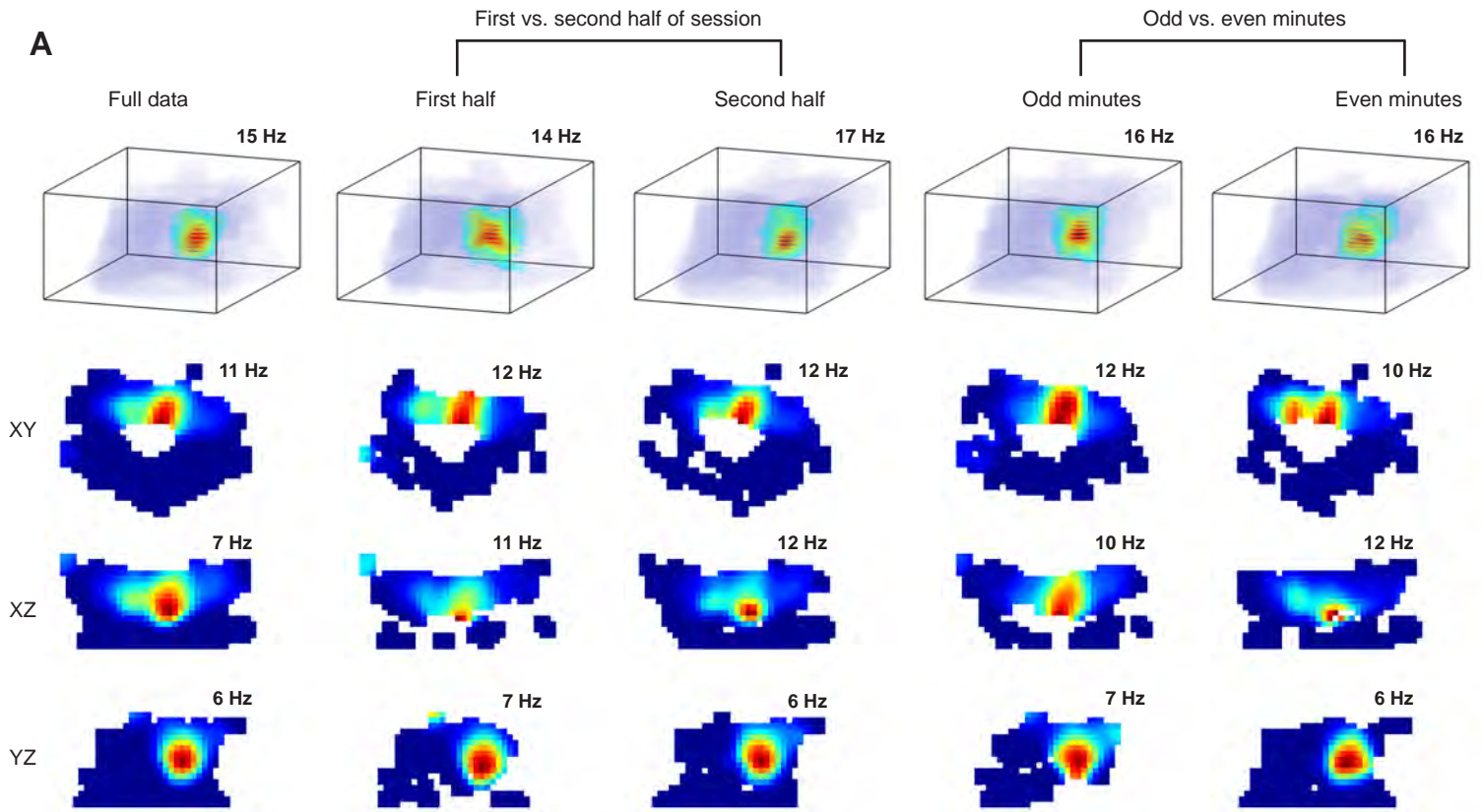
Fig. S14. 3D place fields are stable during the recording session.
Stability of the firing-rate maps of individual place-cells in both experimental setups (the rectangular cuboid flight room and the cubic flight enclosure).   (**A**) Example of 3D rate maps and 2D projections for a single place cell: Column 1: computed over the whole session; Columns 2,3: comparing the rate maps computed over the first and second half of the recording session; Columns 4,5: comparing the rate maps computed over odd minutes versus even minutes (*19*). Same neuron as in Fig. 2 of the main text. Peak firing rate is indicated for each rate-map. Note the stability of the location of the firing field, as well as the stability of the firing-rates across the different comparisons.
(**B**) Distributions of the correlation coefficients for all place cells under the two partitioning conditions (top: odd minutes versus even minutes; bottom: first half versus second half of the session). Data pooled over all the place cells in the two flight setups (rectangular cuboid flight room and cubic flight enclosure; n = 55 cells in total; see also (*19*)).   (**C**) Same as (B), only for place cells which fired ≥ 40 spikes in each of the two partitions of the session. Mean correlation coefficient (average over the neurons) is indicated above each histogram. Bin size, 0.1.
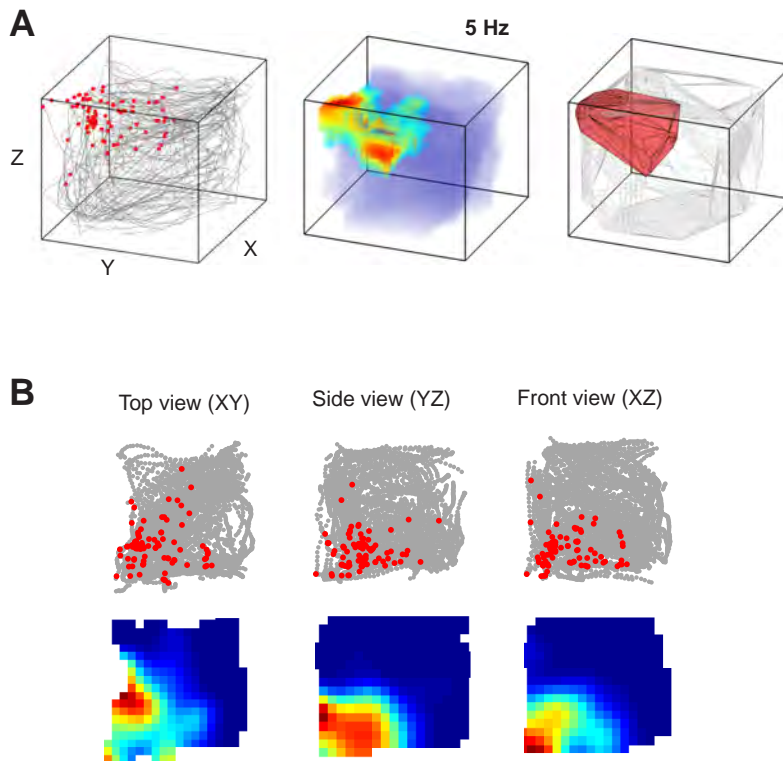
Fig. S15. Example of a 3D place-cell recorded in the cubic enclosure.
(A) 3D representation of the spatial firing of an example place-cell. Left: Spikes (red dots) overlaid on the bat's position (gray line). Middle: 3D color coded firing-rate map; peak rate indicated. Right: Convex hull encompassing the neuron's place field (red polygon) and the volume covered by the bat during flight (gray polygon).
(B) 2D projections for the neuron in (A), showing the raw data (top, gray – animal location, red – spikes) and color-coded rate-maps (bottom).

A

Extraction of voxels above 50% of peak firing rate

fitting an ellipsoid

Delineating the place field

Ellipsoid fitted to the place field

B

Elongation index = c/a
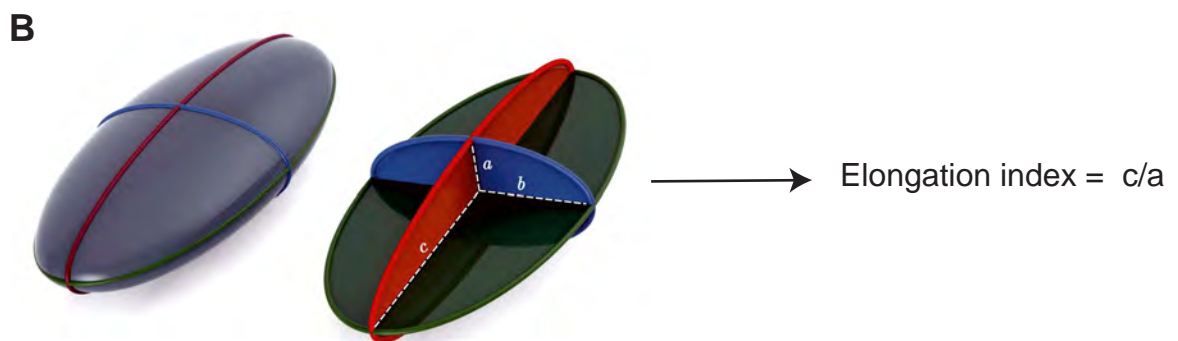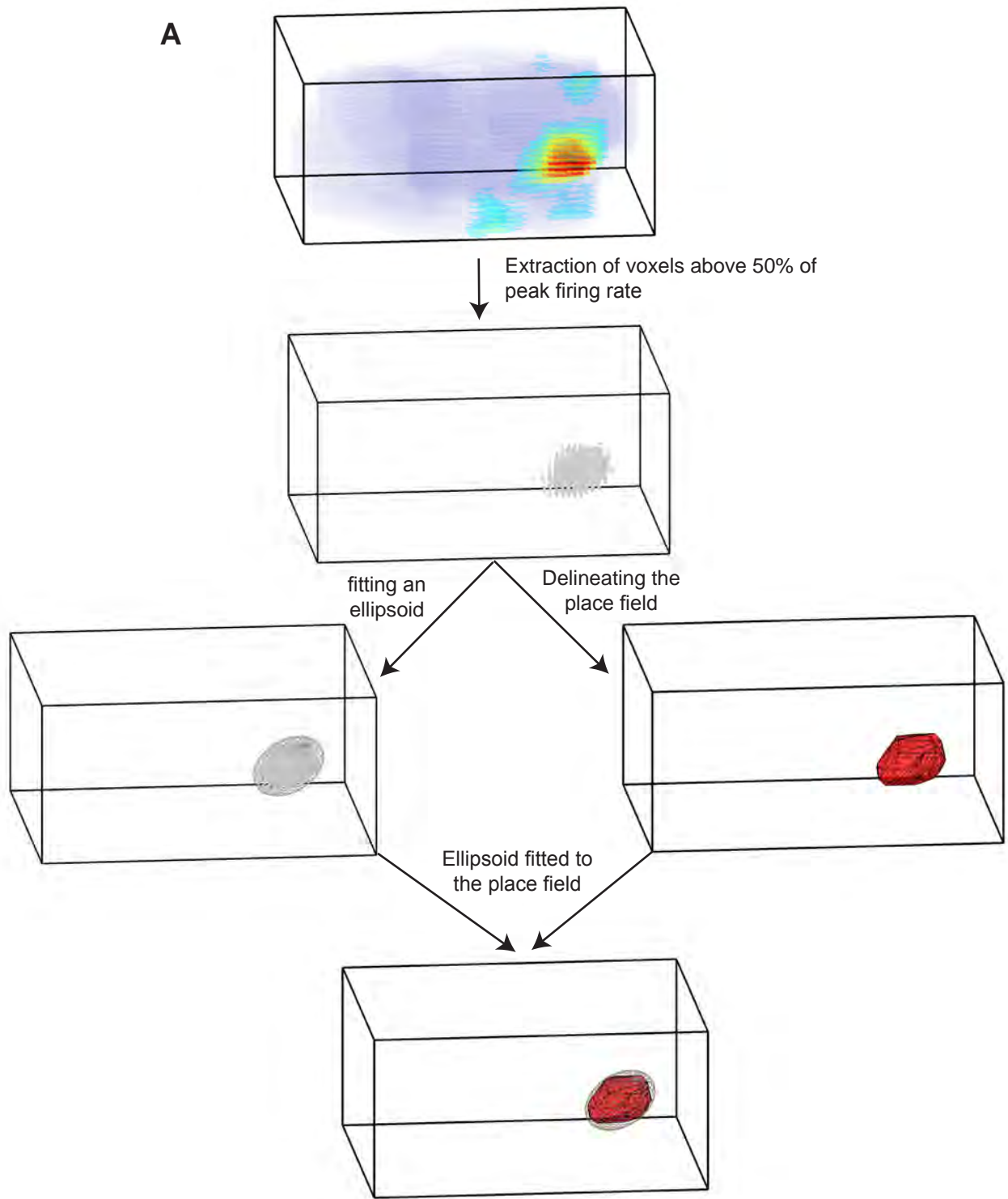
Fig. S16. Computation of the elongation index.
(**A**) Example of fitting an ellipsoid to the place-field of a single neuron. First, taking the 3D rate-map of the neuron (top row), we extract the set of contiguous voxels with firing-rate > 50% of the peak firing-rate, which define a place-field (second row, gray voxels; see details in (*19*)). Subsequently, we fit the place-field with an ellipsoid (third row, left), and in parallel also fit a polygon to the place-field, for display purposes (third row, right; see (*19*)). The ellipsoid is shown overlaid on the polygon in the bottom row. (**B**) The elongation index is computed as the ratio between the longest/shortest axes of the ellipsoid: c / a. The ellipsoid shown in panel (B) is a schematic for illustration only.
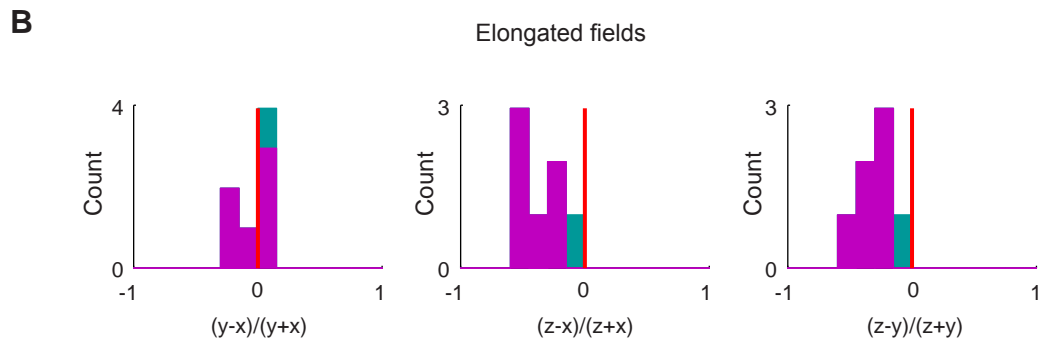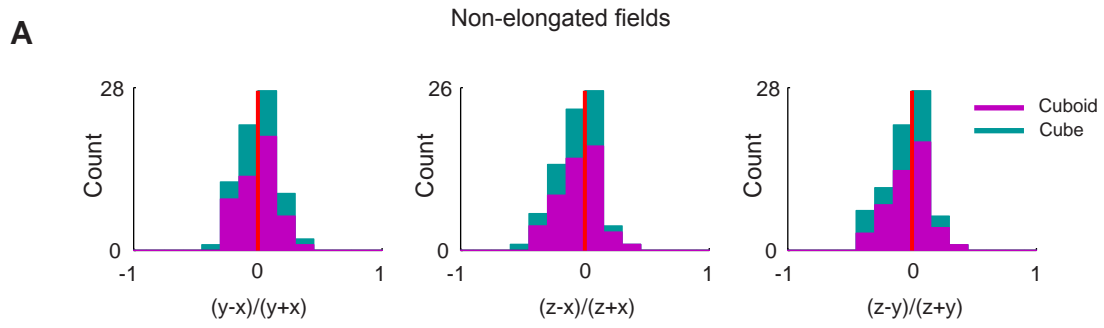
A

Non-elongated fields

B

Elongated fields

C
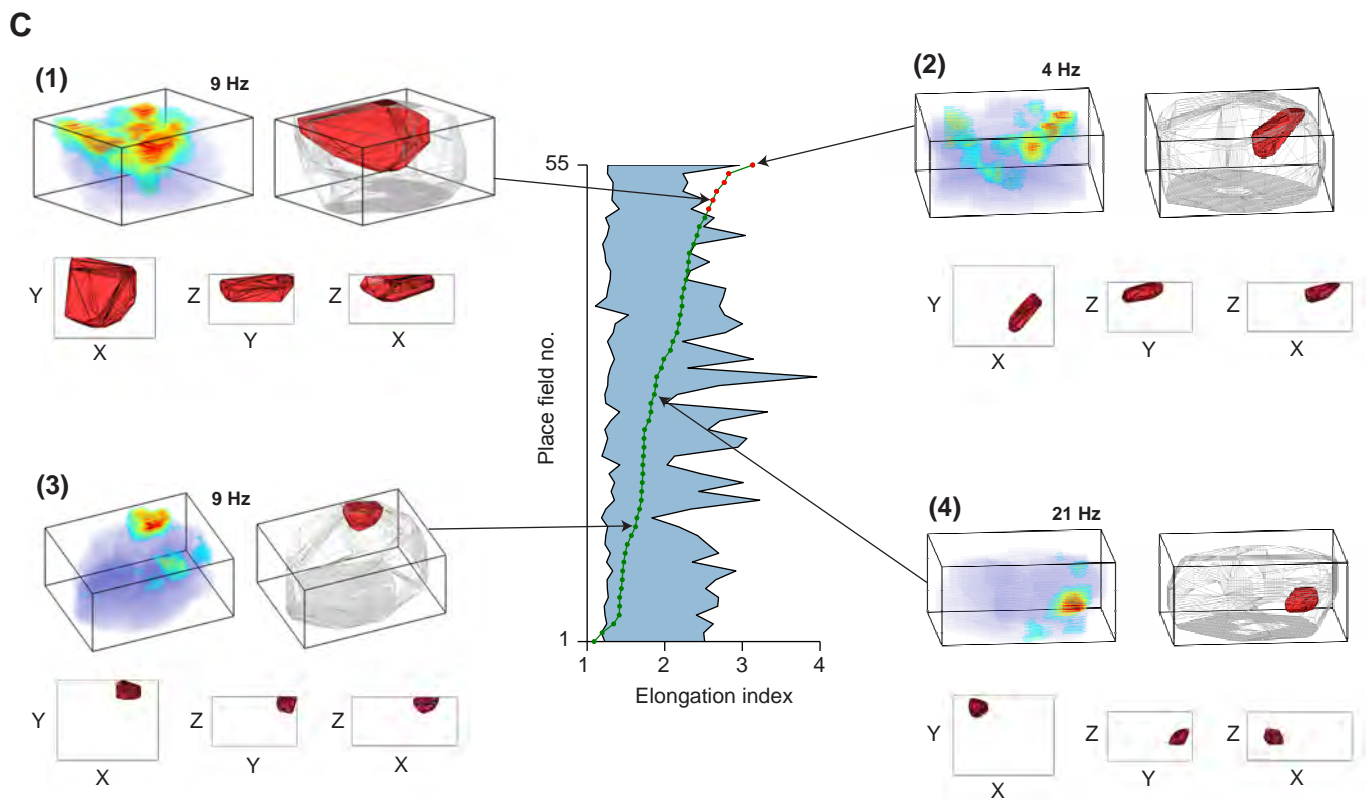
Fig. S17. Contrast indices of cardinal axes for elongated and non-elongated fields.
(A and **B**) Distributions of differential contrast indices (*19*) for all pairs of cardinal axes (major axes: x,y,z), for all the non-elongated place fields (A) and elongated place-fields (B). Data are shown for both the cuboid and cubic experimental setups (colors); bin size, 0.15. Note that for the non-elongated fields shown in A (which are 91% of the total number of recorded place-fields; 75/82 fields), there was no significant elongation in any of the cardinal directions (Sign test, *P* > 0.15 for all comparisons in panel A).   (**C**) Central panel: Elongation indices for all the place-fields in the rectangular-cuboid flight room (*n* = 55 fields), sorted in ascending order. Shaded area, 95% confidence intervals (*19*), same as in Fig. 3I-left. Note that only a small fraction of the fields (red dots) showed significant elongation; these neurons tended to show compression along the z-axis of the room (e.g., neuron #1), but sometimes the fields were also diagonally-shaped (e.g., neuron #2).   However, most place-fields were not significantly different from an underlying sphere (green dots; e.g., neurons #3 and #4). Shown for each of the four neurons are the 3D rate-map (top left); the delineation of the place field (red 3D polygon, top right) superimposed on the flight-volume covered by the bat (gray polygon); as well as 2D projections of the place-field onto the main axes (bottom).
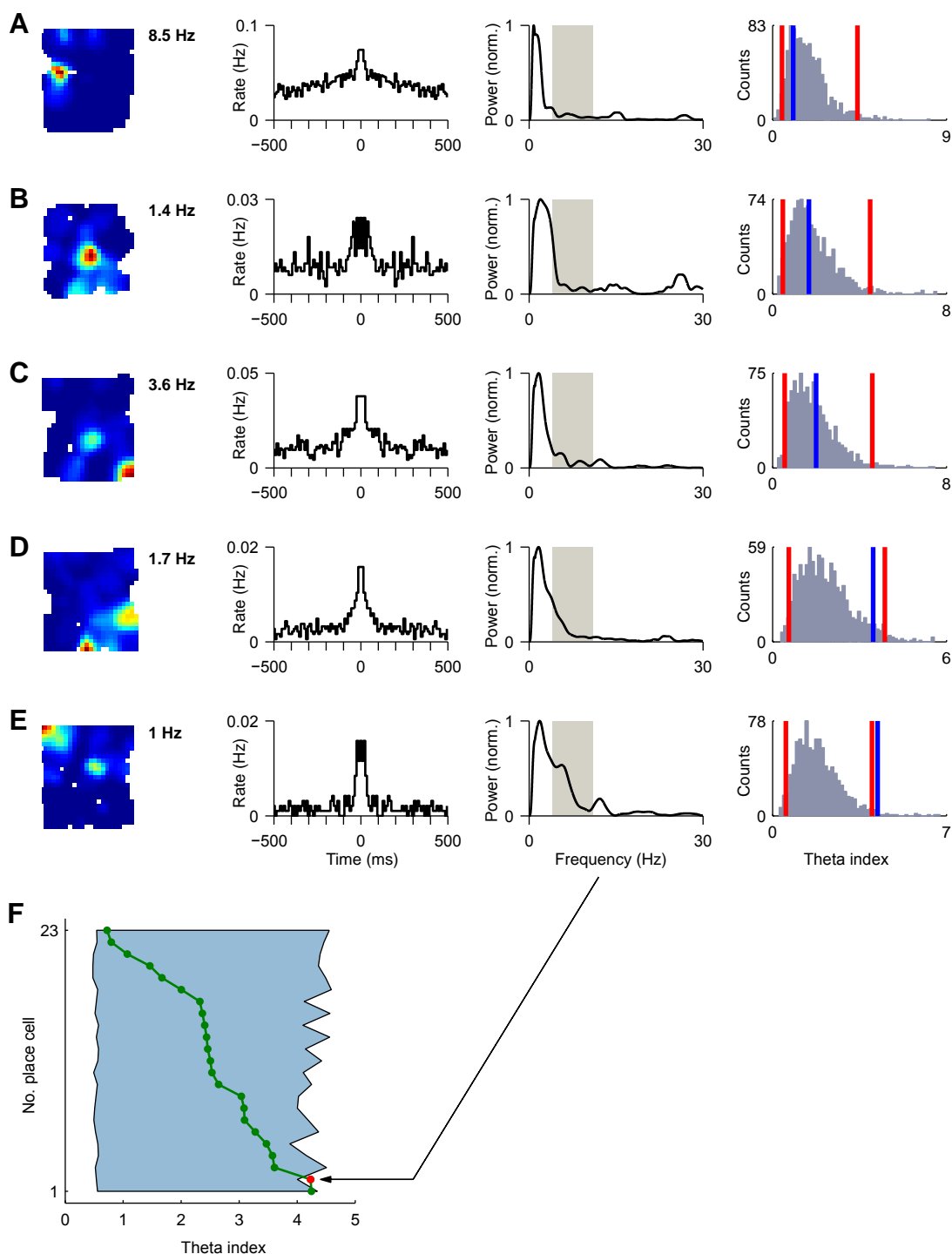
Fig. S18. Near absence of theta rhythmicity in the firing of bat hippocampal place-cells during crawling in a 2D environment. Theta rhythmicity in bat hippocampal neurons is absent also in 2D crawling (re-analysis of the 2D crawling data from ref. *5*). Same notations as Fig. 4 of the main text. (**A** to **E**) Examples of five 2D place-cells. From left to right: 2D color-coded rate maps, with peak firing rate indicated; spike-train temporal autocorrelograms; power spectrum of autocorrelograms; and shuffled distribution of theta-indexes (red lines, 95% confidence intervals; blue line, actual theta-index of the neuron). Note the near absence of spectral power in the theta-band (5-11 Hz, highlighted in gray). The data set is comprised of 23 place cells recorded from hippocampal area CA1 from two crawling Egyptian fruit bats; data are from our previous study, ref. *5*. (**F**) Theta indexes for all place-cells, sorted by increasing theta-index. Shaded area, 95% confidence intervals. Nearly all place-cells were not theta-modulated (green dots, 96% or 22/23 of the place cells not exhibiting significant theta-modulation). The one place-cell that was significantly (albeit weakly) theta-modulated is shown in (E), and is indicated by a red dot in (F).
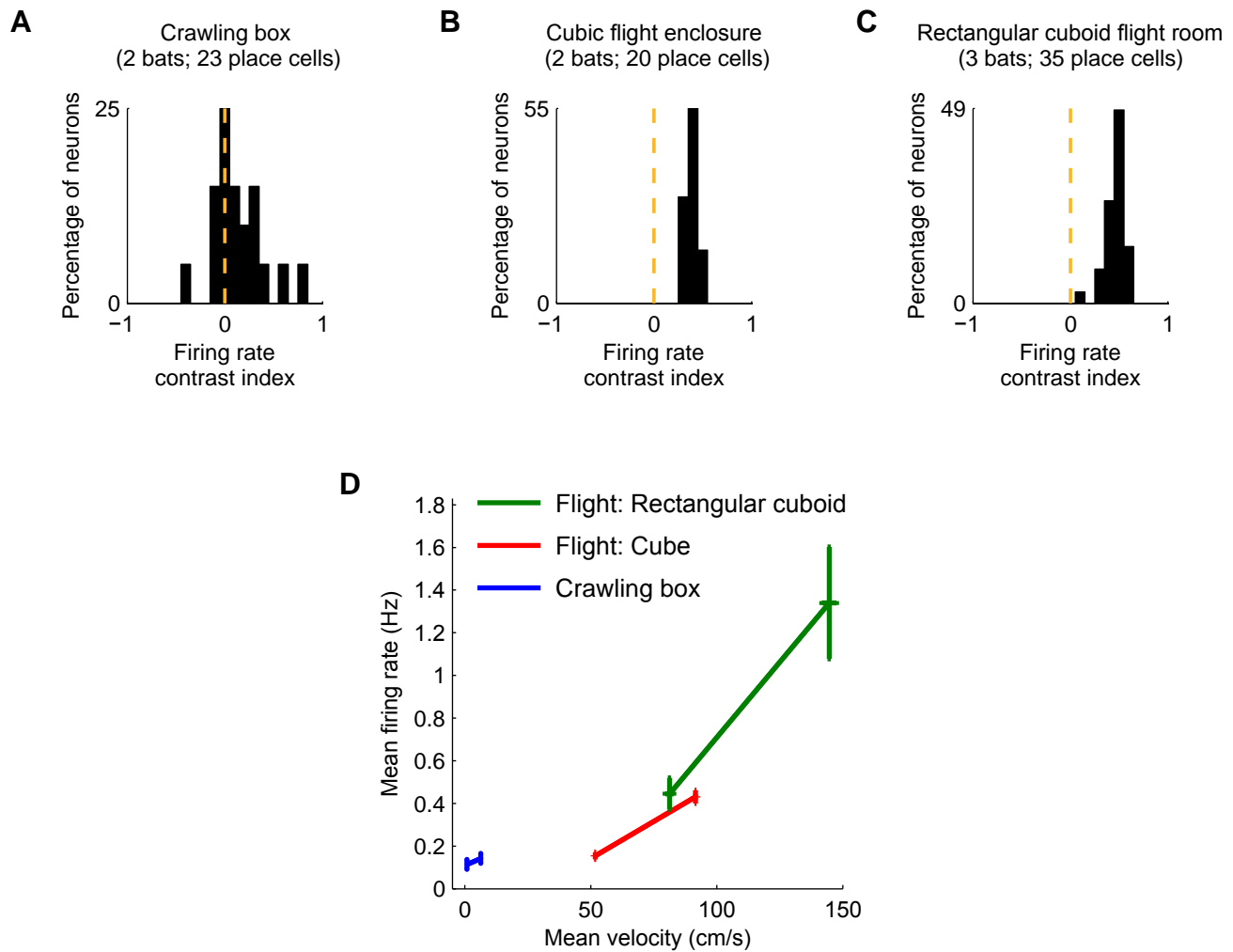
Supplementary Figure 19

Fig. S19. Firing rate of CA1 place cells is modulated by movement velocity.
The effect of the bat's movement velocity on the firing-rate of place cells was assessed by computing the
median velocity for each behavioral session in which a place-cell was recorded, and splitting the video and
spike data into two equally-sized sets of time epochs (in 1-s windows): A high-velocity set (above the
median velocity) and a low-velocity set (below the median velocity). For each of these two sets, we
computed the mean firing-rate, and then computed the contrast index of firing-rates between the high- and
low-velocity, defined as: (FiringRate$_{High}$ − FiringRate$_{Low}$) / (FiringRate$_{High}$ + FiringRate$_{Low}$).
(**A** to **C**) Distribution of firing-rate contrast indexes for high versus low movement velocity across three
different experimental setups: (A) Crawling in a 1.17 x 1.17 m² box (data from ref. *5*). (B) Flying in the 2.9
x 2.8 x 2.7 m³ cubic enclosure. (C) Flying in the 5.8 x 4.6 x 2.7 m³ rectangular cuboid room. Note that in
all cases, but especially in the two flight setups, the distributions are strongly skewed towards positive
values, indicating that the firing-rate of place cells increases with velocity. (D) Summary graph showing the
mean firing rate versus mean movement velocity for the 3 setups (3 colors), and for the high versus low
velocities within each setup (the two error-bars in each color; mean ± s.e.m.). Note that, first, the mean
firing-rate is much higher in flight (green and red) compared to crawling (blue); second, firing-rate increased
substantially with the size of the available flight enclosure, where the bats can reach higher movements
velocities (compare green versus red); third, firing-rate increased with velocity within each experimental
setup (all 3 colored lines have positive slopes).

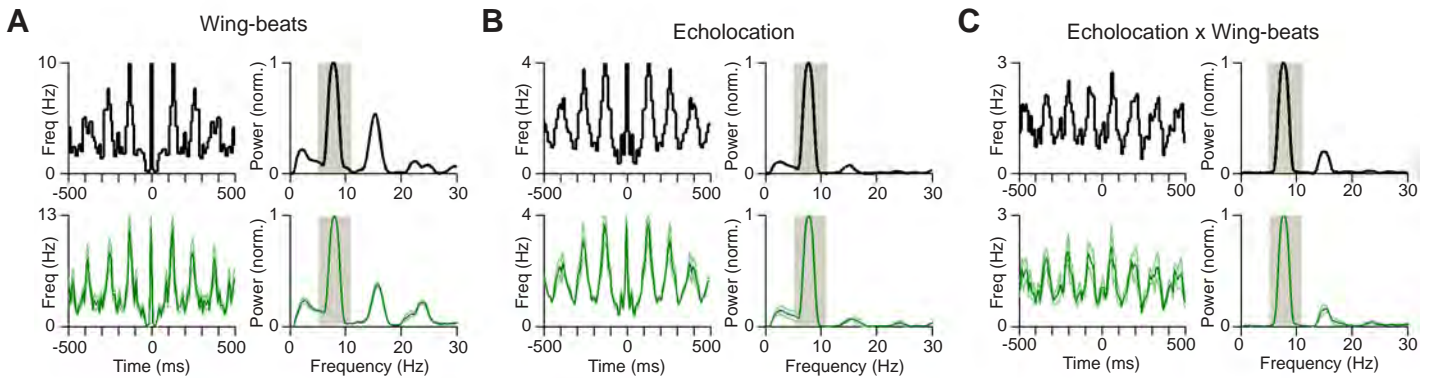**Fig. S20. Behavioral oscillations in freely flying bats.**
(**A** and **B**) Examples (top) and population averages (bottom, mean ± s.e.m., green) of temporal autocorrelograms (left) and power-spectrum (right) of the bat's wing-beats (A) and echolocation (B). Note the clear rhythmicity in the autocorrelograms, and the pronounced spectral peak of these behaviors at the theta frequency (5–11 Hz, gray rectangle). Power normalized to 1.
(**C**) Cross-correlation of wing-beats and echolocation calls, showing phase-locking. The examples in (A to C, top) are all from the same behavioral session, in the rectangular cuboid flight-room.
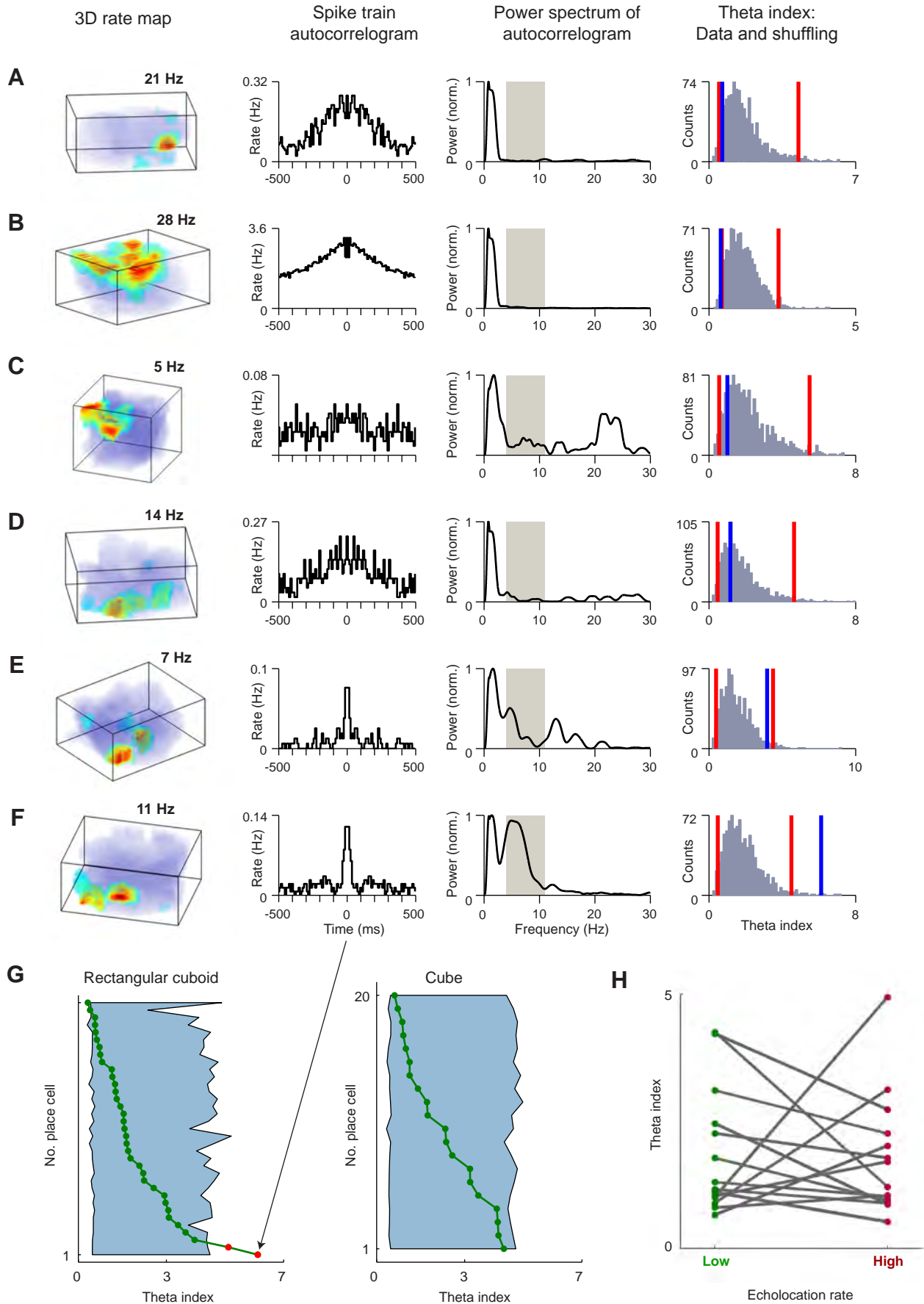
Fig. S21. Near absence of theta rhythmicity in the firing of bat hippocampal place-cells during flight. (**A** to **F**) Six example cells. From left to right: 3D color-coded rate maps, with peak firing-rate indicated; spike-train temporal autocorrelograms; power spectrum of autocorrelogram (mean-removed); and shuffled distribution of theta-indexes (red lines, 95% confidence intervals; blue line, actual theta-index of the neuron; see also (*19*)). Note near absence of power in the theta-band (5–11 Hz, gray rectangle in the third column; power normalized to 1). The cell shown in (F) was the most theta modulated place-cell in our dataset (arrow) – but this neuron exhibited, in fact, quite a weak oscillation in its temporal autocorrelogram (compare to the very strong theta-rhythmicity observed in rats or mice, e.g., refs *23*, *24*). (**G**) Theta indexes for all place-cells from both experimental setups. Left: Rectangular-cuboid flight room (*n* = 35 cells). Right: Cubic flight enclosure (*n* = 20 cells). Neurons sorted by their theta-index values. Shaded area, 95% confidence intervals. Only a small fraction of place-cells (3.6%, 2/55 neurons in both setups together) were significantly theta-modulated (red dots), while nearly all of the place cells (96.4%, 53/55 neurons) were not theta-modulated (green). (**H**) Theta modulation is not dependent on echolocation rate in flying bats: Theta indexes were computed separately for each place-cell (14 place-cells recorded simultaneously with audio data) for low and high echolocation rates. Each line corresponds to a single place cell; 'low' and 'high' echolocation rate were divided based on the median echolocation-rate in each recording day. Note that this result in flying bats seems, at first, different from our previous finding in crawling big brown bats, in which theta power (LFP) increases with echolocation-rate (ref. *3*). The difference is likely due to the fact that in flight, echolocation-rate and flight velocity are correlated (due to the phase-locking between echolocation rate and wingbeat-rate; see fig. S20), and therefore the flight-mode is more akin to the "exploration by locomotion" mode in our previous study in crawling bats (ref. *3*), during which theta was in fact *not* found in the big brown bat – similar to our finding here in the flying Egyptian fruit bat.
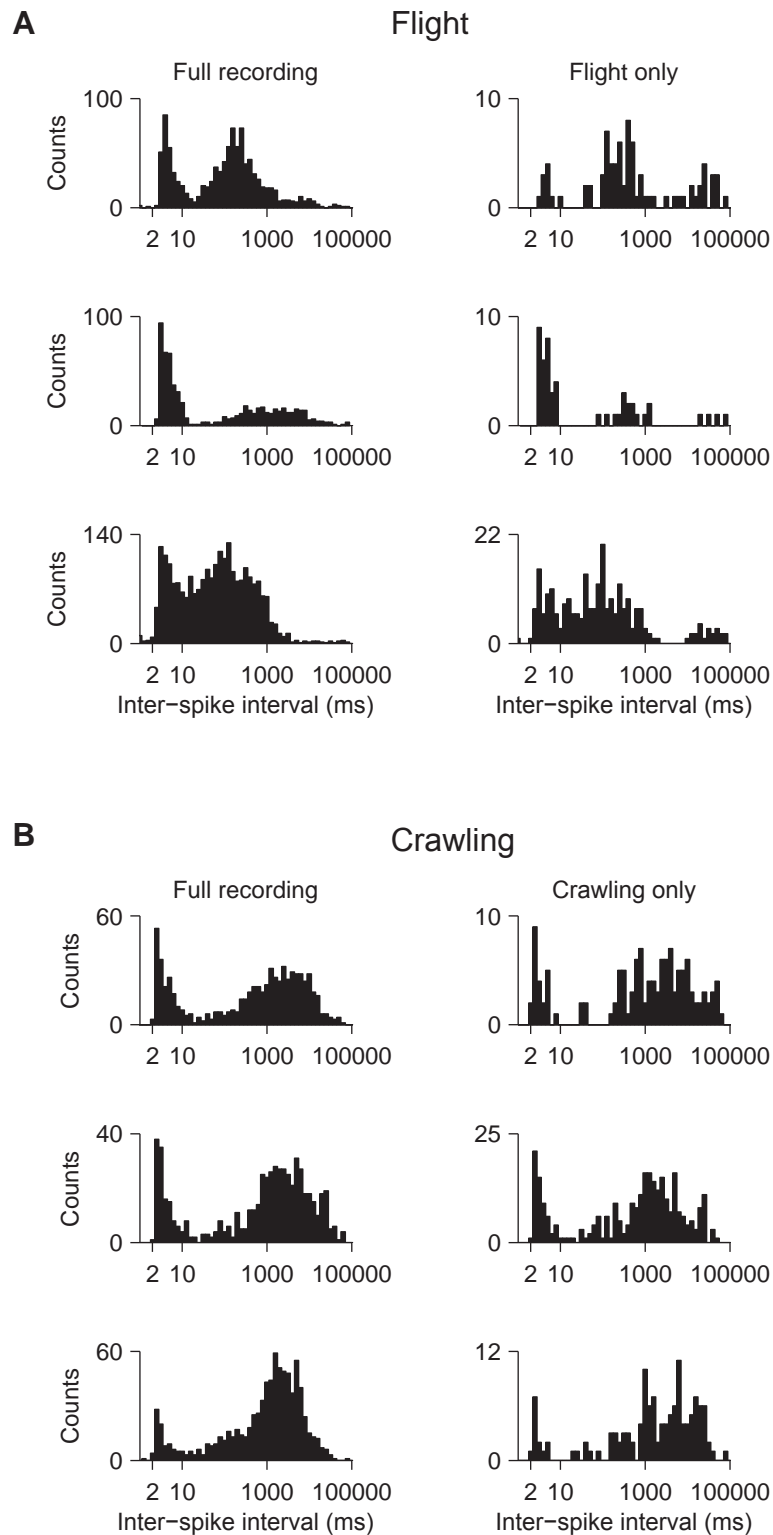
Supplementary Figure 22

Fig. S22. **Inter-spike interval distributions for hippocampal CA1 neurons during flight and crawling.** Inter-spike interval histograms of 3 example CA1 neurons recorded during flight (**A**) and additional 3 CA1 neurons recorded during crawling (**B**). Crawling data from ref. *5*. Each row depicts one neuron. Distributions are shown separately for the entire recording of each neuron (including behavioral and sleep sessions, left column), as well as exclusively for periods of active flight (A, right column) or active crawling (B, right column). Note the bimodality of the inter-spike interval distributions of these CA1 neurons, with a peak at small inter-spike intervals (approximately 2-10 ms) – suggesting pronounced complex-spike bursts, as expected from hippocampal CA1 pyramidal cells.

Supporting References

S1. J. D. Altringham *Bats: Biology and Behaviour* (Oxford University Press, Oxford, 1996).

S2. G. Neuweiler, *The Biology of Bats* (Oxford University Press, Oxford, 2000).

S3. Y. Yovel, B. Falk, C. F. Moss, N. Ulanovsky, *Science* **327,** 701 (2010).

S4   Y. Yovel, M. Geva-Sagiv, N. Ulanovsky, *J. Comp. Physiol. A* **197,** 515 (2011).

S5. Y. Yovel, B. Falk, C. F. Moss, N. Ulanovsky, *PLoS. Biol.* **9,** e1001150 (2011).

S6. R. A. Holland, D. A. Waters, *Acta Chiropt.* **7,** 83 (2005).

S7. R. A. Holland, P. Winter, D. A. Waters, *Ethology* **111,** 715 (2005).

S8. N. Schmitzer-Torbert, J. Jackson, D. Henze, K. D. Harris, A. D. Redish, *Neuroscience* **131,** 1 (2005).

S9. J. C. Jackson, A. Johnson, A. D. Redish, *J. Neurosci.* **26,** 12415 (2006).

S10. C. N. Boccara *et al.*, *Nat. Neurosci.* **13,** 987 (2010).

S11. W. E. Skaggs, B. L. McNaughton, M. A. Wilson, C. A. Barnes, *Hippocampus* **6,** 149 (1996).

S12. W. E. Skaggs, B. L. McNaughton, M. A. Wilson, E. J. Markus, in *Advances in neural information processing systems 5,* S. J. Hanson, J. D. Cowan, C. L. Giles, Eds. (Morgan Kaufman, San Mateo, 1993), pp. 1030-1037.

S13. S. S. Deshmukh, D. Yoganarasimha, H. Voicu, J. J. Knierim, *J. Neurophysiol.* **104,** 994 (2010).